ornl

ORNL/TM-10719

OAK RIDGE NATIONAL LABORATORY

MARTIN MARIETTA

Transient Thermal Analysis of Three Latent Heat Storage Configurations for Rapid Thermal Charging

T. K. Stovall

OPERATED BY
MARTIN MARIETTA ENERGY SYSTEMS, INC.
FOR THE UNITED STATES
DEPARTMENT OF ENERGY

Printed in the United States of America. Available from
National Technical Information Service
U.S. Department of Commerce
5285 Port Royal Road, Springfield, Virginia 22161
NTIS price codes—Printed Copy: A05 Microfiche A01

ORNL/TM-10719

Engineering Technology Division

TRANSIENT THERMAL ANALYSIS OF THREE LATENT HEAT STORAGE CONFIGURATIONS FOR RAPID THERMAL CHARGING

Therese K. Stovall

Date Published - May 1988

Prepared by the
OAK RIDGE NATIONAL LABORATORY
Oak Ridge, Tennessee 37831
operated by
MARTIN MARIETTA ENERGY SYSTEMS, INC.
for the
U.S. DEPARTMENT OF ENERGY
under Contract No. DE-AC05-840R21400

TABLE OF CONTENTS

LIST OF FIGURES

LIST OF TABLES

NOMENCLATURE

A	area, m^2
A_c	area of finite difference grid element face perpendicular to cylinder axis, m^2
A_{pin}	area of finite difference grid element face parallel to cylinder axis and closest to center of cylinder, m^2
A_{pout}	area of finite difference grid element face parallel to cylinder axis and farthest from center of cylinder, m^2
α	thermal diffusivity, m^2/s
c_p	specific heat, J/g-°K
c_ℓ	specific heat (liquid) J/g-°K
c_s	specific heat (solid) J/g-°K
d_h	hydraulic diameter, $2(R_f - R_o)$
E	internal energy, J/g
Fo	Fourier number, $\alpha\tau/R^2$
h	heat transfer coefficient, W/m^2-°K
i	enthalpy, J/g
i_s^*	enthalpy in the solid saturated state, J/g
k	thermal conductivity, W/m-°K
k_ℓ	thermal conductivity (liquid), W/m-°K
k_s	thermal conductivity (solid), W/m-°K
k_w	tube wall thermal conductivity, W/m-°K
L	length of PCM cylinder, m
L_f	latent heat of fusion, J/g
M	number of radial divisions in finite difference grid
$\dot{m}$	flow rate of liquid metal, g/s

N	number of axial divisions in finite difference grid
NPIPES	number of PCM cylinders
Nu_x	Nusselt number, hx/k
PCM	phase change material
Pe	Peclet number, VL/α
Pr	Prandtl number, $\mu * c_p/k$
q	thermal energy flow, J/s
r	radial coordinate, m
R(τ)	radial position of the phase change front, m
Re	Reynolds number, vx/ν
R_f	radius of liquid metal boundary, m
ρ	density
R_o	radius of PCM cylinder, m
Ste	Stefan number, $c_s\ (T_m - T_{init})/L_f$, dimensionless
T	temperature, °K
τ	time, seconds
τ_d	test duration, seconds
T_{avg}	average of maximum inlet and outlet liquid metal temperatures, °K
T_{in}	maximum inlet temperature of liquid metal, °K
T_{init}	initial temperature, °K
T_{out}	maximum outlet temperature of liquid metal, °K
T_m	melting temperature of PCM, °K
t_w	wall thickness, m
U	Kirchoff temperature, defined in Sect. 3.1

V	volume, m^3
$\dot{W}_t$	thermal load, W
x	volume fraction of enhancement material added to PCM
z	axial coordinate, m
θ	dimensionless enthalpy, defined in Sect. 3.1
θ^*	dimensionless energy storage, defined in Sect. 3.1
ϕ	dimensionless temperature, defined in Sect. 3.1

ACKNOWLEDGMENTS

I would like to thank my project sponsor, Mitch Olszewski, for the opportunity to do this work and my major professor, Rao Arimilli, for his many hours of review and suggestion. I would also like to thank my other advisory committee members, Profs. Parang and Keshock, for their helpful comments. Two typists, Lynn Crawley and Debbie Milsap, and three graphic artists; Shawna Parrot, Margaret Eckerd, and Vicki Beets, helped me to generate this paper in a very short time frame. Most importantly, I would like to thank my husband, John Stovall, who took care of the children so I could complete this work.

ABSTRACT

A space-based thermal storage application must accept large quantities of heat in a short period of time at an elevated temperature. An approximate model of a lithium hydride phase change energy storage system was used to estimate reasonable physical dimensions for this application which included the use of a liquid metal heat transfer fluid. A finite difference computer code was developed and used to evaluate three methods of enhancing heat transfer in the PCM energy storage system. None of these three methods, inserting thin fins, reticulated nickel, or liquid lithium, improved the system performance by a significantly large amount. The use of a 95% void fraction reticulated nickel insert was found to increase the storage capacity of the system slightly with a small decrease in the system energy density. The addition of 10% liquid lithium was found to cause minor increases in both storage density and storage capacity with the added benefit of reducing the hydrogen pressure of the lithium hydride.

1. INTRODUCTION

1.1 Project Purpose

A space-based power system application requires a large amount of heat rejection from a power cycle in a short period of time. One proposed solution is to use a phase change thermal energy storage system to absorb the rejected heat and then release it to space over a longer period of time. The basic arrangement of the proposed storage system consists of a cylindrical tube filled with a phase change material with a high melting temperature surrounded by an annular region containing the liquid metal heat transport fluid. Lithium hydride is the preferred thermal energy storage medium because of its high latent heat and thermal conductivity and because its melt temperature matches the needs of the application well.

Similar systems have been modeled in the past. However, the short time constraints for this application, coupled with the poor thermal diffusivity of the medium, have led to the consideration of three heat transfer enhancements. The enhancements considered include: 1) the addition of thin fins, 2) the insertion of a solid lattice of reticulated nickel, and 3) the addition of a molten metal to a like metal salt (lithium and lithium hydride). In this third enhanced system, the metal is always a liquid and the salt melts and freezes, forming a slush-like material. The reticulated nickel lattice is similar to a steel wool pad inserted into the PCM tube before the PCM material is poured in.

This research is part of a larger effort with other researchers investigating two related areas. The first is the formation of voids within the phase change medium caused by changes in density (assumed constant in the present study) and the influence of a gravity-free environment on the location of such voids. The second is the performance of a packed bed of encapsulated phase change material.

The primary focus of this project is to define a baseline latent thermal energy storage system and compare its performance to three enhanced latent thermal energy storage systems. An existing computer code was substantially modified to reflect the requirements of this task. Chapter 2 describes an approximate analysis that was used to estimate feasible system configurations. In Chap. 3, the computer model of the system is described and the results for the enhanced systems are compared in Chap. 4. The conclusions from this comparison and recommendations for future study are presented in Chap. 5.

1.2 Problem Definition

At this time, the energy storage requirements for the application have been only tentatively defined and are subject to change. The power source may range in size from 10 to 5,000 MW and may operate over a time period of 200 to 1,500 seconds [1]. For this study, a thermal storage system was sought to accept the rejected heat from a constant power source of 250 MWe (generated with a thermal efficiency of 25%) for an operational period between 900 and 1000 seconds. The thermal energy that must be stored is therefore approximately

7.5×10^{11} J. The storage system is composed of a system of tubes filled with PCM that receives the rejected heat from hot liquid metal flowing on the shell side, see Fig. 1.1. The maximum tube length permitted is about 5 m. The maximum allowable liquid metal temperature leaving the PCM storage system is 1100°K and the maximum inlet liquid metal temperature is 1200°K. The initial temperature of the PCM system is 700°K. The tube walls are made of 304SS with a tube wall thickness of about 1.27E-4 m (0.005 in.) [2]. The properties of the liquid metal, tube wall, and PCM are shown in Table 1.1.

An individual PCM cylinder surrounded by liquid metal is modeled for this analysis, see Fig. 1.2. The PCM cylinders are radially symmetric with insulated ends. The outer boundary of the liquid metal annular volume is assumed to be adiabatic by symmetry. Dwyer presented a full discussion on the use of such an equivalent circular

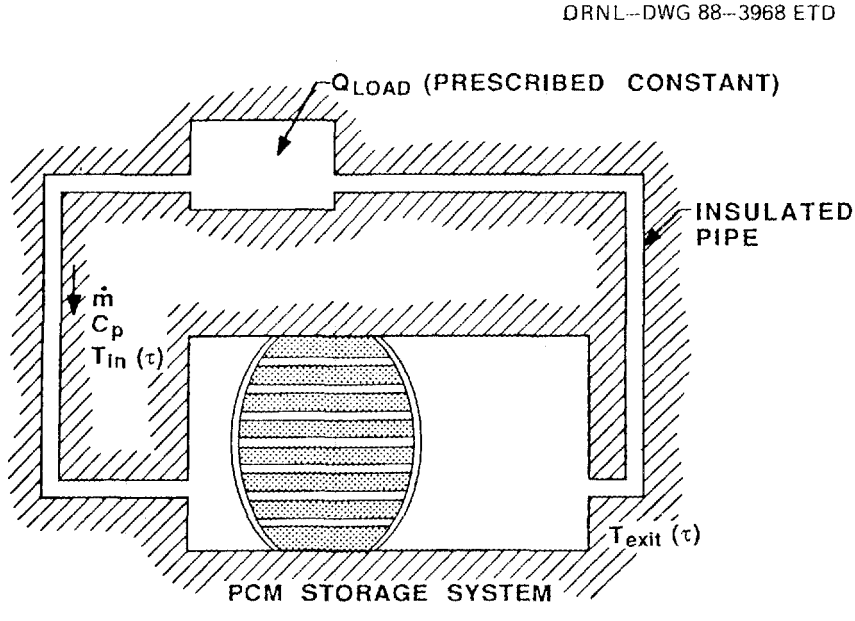

Fig. 1.1. System Schematic.

Table 1.1. Material Properties

Property	Value
Liquid metal[a]	
k	28.9 W/m-°K
c_p	1.043 J/g-°K
ρ	7.401×10^5 g/m^3
μ	0.161 g/m-s
Lithium hydride[b]	
ρ[c]	5.5×10^5 g/m^3
k (solid)	4.18 W/m°K
k (liquid)	2.51 W/m°K
c_p (solid)	8.33 J/g°K
c_p (liquid)	7.36 J/g°K
L_f	2845 J/g
T_m	962 °K
Tube wall[d]	
ρ	7.803×10^6 g/m^3
k	24.2 W/m-°K
c_p	0.46 J/g-°K

[a] Na (56%) K (44%) at 704°C (977°K) [3, p. 564].

[b] [4].

[c] Assumed constant for both solid and liquid states.

[d] 304SS steel (18% C, 8% Ni) [3, p. 541].

boundary for triangular arrays of tubes with wide spacing (R_f/R_o > 1.35) [5, p. 104-105]. His methods could be used to facilitate the extension of the results of this study to a full bank of such tubes.

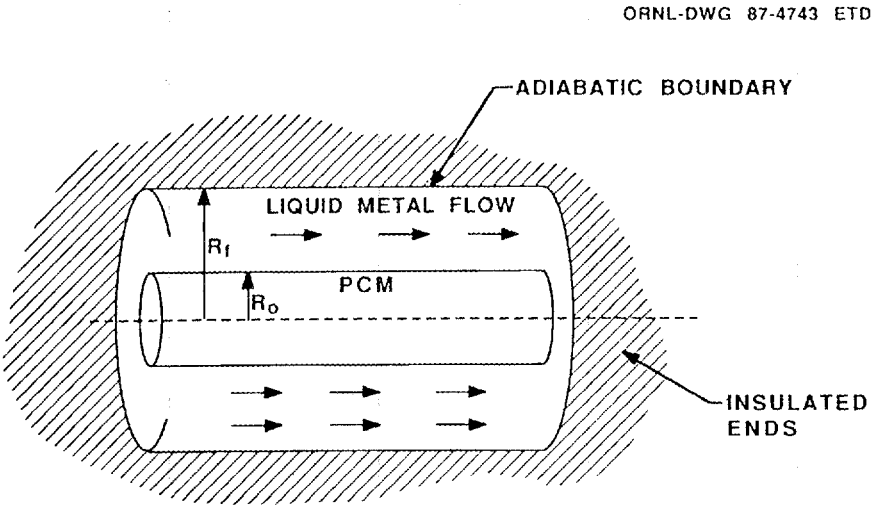

Fig. 1.2. Model Schematic.

1.3 Literature Review

The use of a hollow cylinder of PCM for latent energy storage was modeled by Solomon et al. and is described in Ref. 6. He used a finite difference formulation with the Kirchoff temperature to calculate the internal energy, temperature, and the position of the phase change front. The Kirchoff temperature approach is also used in this analysis and is described more fully in Sect. 3.1. Solomon also used a quasi-steady approximation method to estimate reasonable values for input to the more exact finite difference model. A very similar quasi-steady approximation was used in this effort and is reported in Sect. 2.1. Solomon's work and this analysis differ in four major areas: 1) geometry, 2) heat transfer material, 3) the charging requirements, and 4) the use of heat transfer enhancements. Solomon's geometry consisted of a hollow cylinder of PCM with a gaseous heat transfer medium flowing through the center of the cylinder. The charge and discharge cycles were attuned to a solar cycle. Because

the charging times were so long, the poor conductivity of the PCM was of less concern and enhancements were not considered.

The enthalpy method of analysis was rigorously verified for a phase change application by Shamsundar and Sparrow [7]. Using an integral formulation, they show that the enthalpy approach is identical to the more classical approach and that knowledge of the location of the phase change front is not necessary for the solution. Shamsundar and Sparrow also defined dimensionless parameters useful for phase change problems and formulated the conservation equation in terms of these variables. These variables are described in Sect. 3.1 and are used in the presentation of results in Sect. 4.2.

A useful text in the area of finite difference problem solutions was written by Dusinberre [8]. This text includes an especially clear discussion of time-step size requirements for stability.

Knowles and Webb [9] have examined the use of a mixed enthalpy model for metal/PCM composities both analytically and experimentally. Their thermal model is based on volume-average effective thermal parameters which are used in Sect. 3.4 of this report.

Several heat transfer correlations for liquid metal flowing in an annulus were available in the literature. Some of these were based on theoretical considerations and others on experimental data.

Dwyer's theoretical derivation for laminar flow was based on the following assumptions: heat transfer from the inner wall only, uniform heat flux, negligible axial heat conduction, and fully developed velocity and temperature profiles [10]. This analysis showed the Nusselt number and bulk fluid temperature to be a function of the

ratio, R_f/R_o. The results were presented in tabular form, some of which are listed in Table 1.2 (excerpted from Dwyer, [10], p. 337). The simplistic relation between geometry and Nusselt number in this correlation made it an attractive choice for the approximate analysis. These results were therefore used in the approximate analysis in the form of Eq. 2.10 in Sect. 2.2 for R_f/R_o ratios from 1.2 to 3.0.

Table 1.2. Nusselt Numbers and Wall and Bulk Temperature Relationships for Flow Through Annuli[a]

R_f/R_o	Nu	$\frac{T_1 - T_b}{T_1 - T_2}$[b]
1 (parallel plates)	5.385	0.743
1.25	5.60	0.758
1.50	5.78	0.771
2.00	6.17	0.790
4.00	7.78	0.832
6.00	9.22	0.856
8.00	10.57	0.870
10.00	11.90	0.879
∞ (round pipes)	∞	1.000

[a] Excerpted from Dwyer [10, p. 337] for laminar flow with heat transferred from the inner wall only.

[b] T_1 = inner wall temperature, T_b = liquid metal bulk temperature, and T_2 = outer wall temperature.

Dwyer ([10], p. 340) also provided a correlation (Eq. 1.1) applicable to either laminar or turbulent flow in an annulus under conditions of fully developed flow and uniform heat flux.

$$Nu = 4.82 + 0.697\ y + 0.0222\ (\psi Pe)^{(0.758\ y^{0.053})} \qquad \text{(Eq. 1.1)}$$

where

$y = R_f/R_o$

ψ = dimensionless average value of ratio, $\varepsilon_H/\varepsilon_m$

$\varepsilon_H = K_e/\rho c_p$ = eddy diffusivity of heat transfer

$\varepsilon_m = \mu_e/\rho$ = eddy diffusivity of momentum transfer

K_e = eddy thermal conductivity

μ_e = eddy dynamic viscosity

Another heat transfer correlation was based on empirical data (Duchatelle [11,12,13]) for a heat exchanger with NaK flowing in an annular space. The reported experimental results cover a range of Peclet numbers from 500 to 3000. The authors extrapolate the relation down to a Peclet number of 40 in comparing their results to those of other authors. This correlation was chosen for use in the finite difference code because this range is appropriate for the modeled flow with a Peclet number of about 200. In Duchatelle's correlation (Eq. 1.2), the Nusselt and Peclet numbers are based on the hydraulic diameter $[2(R_f-R_o)]$ and the liquid metal physical properties are taken at the bulk average temperature. Duchatelle also uses a temperature dependent conductivity, unlike the constant value used in this study. The value F in Eq. 1.2 is a factor to increase the heat transfer coefficient in the thermal and hydraulic establishment length and is shown in Eq. 1.3. For an R_f/R_o ratio of 2 and a ψ value of 1, Eqs. 1.1 and 1.2 are nearly equivalent.

$$Nu = (6.15 + 0.02\ Pe^{0.8})\ F \quad \text{for } 40 < Pe < 3000 \qquad \text{(Eq. 1.2)}$$

$$F = 0.194 \left(Pe \frac{d_h}{L} \right)^{0.49} \qquad \text{for } \frac{Ped_h}{L} > 28$$

$$F = 1 \qquad \text{for } \frac{Ped_h}{L} < 28 \qquad \text{(Eq. 1.3)}$$

Another equation (Eq. 1.4) was theoretically derived for liquid metal flow across a flat plate but showed good comparison to experimental data for a flow of liquid metal along the surface of an unbroken section of tubing [14].

$$\overline{Nu} = 0.46 \, (Pe)^{0.65} \quad \text{for } 10^3 \leq Pe \leq 10^5 \qquad \text{(Eq. 1.4)}$$

Yet another correlation was presented by Subbotin [15,16] for a forced-convection sodium film coefficient for a bank of tubes, Eq. 1.5. In this formula, the variable "S" is the distance from the center of one tube to the center of an adjacent tube. The ratio of S to $2R_o$ is therefore analogous to the ratio R_f/R_o in the model studied in this report. The correlation in Eq. 1.5 is applicable for $1.1 < S/2R_o < 1.4$ and for $200 < Pe < 1200$. There are also some restrictions on the length to diameter ratio. For the geometry of the configurations modeled in this report, the Subbotin Nusselt number estimate is about 25% less than that based on Duchatelle's correlation. However, the R_f/R_o ratio in this configuration equals three and is beyond Subbotin's limits. If configurations with smaller radius ratios are modeled, this correlation should be considered.

$$Nu = 8 \left[\frac{d_h}{L} + 0.27 \left(\frac{S}{2R_o} - 1.1 \right)^{0.46} \right] Pe^{0.6} \qquad \text{(Eq. 1.5)}$$

2. PRELIMINARY CONFIGURATION SELECTION

An approximate analytical solution for this problem was used to determine potential system configurations. The parameters that must be coordinated in such configurations include: PCM cylinder radius, liquid metal annulus radius, liquid metal velocity, tube length, and number of cylinders required.

The PCM and liquid metal regions are estimated separately in Sects. 2.1 and 2.2 and the two approximate solutions are then coupled in Sect. 2.3 through their common geometrical boundaries and the convective heat transfer coefficient. The approximate solution resulted in a small self-contained computer code, independent of the finite difference code. It should be noted that the performance of the resulting configurations was evaluated using the finite difference code. Modifications to the configurations were then made based on this evaluation.

2.1 Approximate Model for the Phase Change Material Region

The PCM approximate model is patterned very closely after the one introduced by Solomon [6]. Solomon used a quasi-steady formulation to allow a simplified analysis. This approach is discussed more fully in Arpaci and Larsen [17, p. 181]. A quasi-steady formulation involves neglecting unsteady terms in at least one, but not all, of the governing equations of an unsteady problem. The application of the quasi-steady simplification is most appropriate when the phase growth is very slow and the sensible heat storage is much smaller than the latent heat storage. This is therefore a reasonable approximation for

cases where the Stefan number is less than or equal to one (see Arpaci and Larsen [17, p. 176]). This simplification ignores the heat addition required to steadily heat the liquefied layer as it grows in thickness.

The model considered consists of an axisymmetric PCM cylinder of outer radius R_o, initially solid at its melting temperature. The surface is exposed to convective heat transfer from a liquid metal flowing at a constant temperature. The heat transfer coefficient is assumed to be a known quantity during this portion of the analysis and is discussed more fully in Sect. 2.3. A phase change front, $R(\tau)$, separates the liquid PCM ($r > R(\tau)$) from the solid PCM ($r < R(\tau)$) (see Fig. 2.1). In both this approximate solution and in the finite difference solution, the PCM density is assumed to remain constant, i.e. the density is unaffected by state or temperature. Also, there is assumed to be no motion (i.e. no convection) within the liquid PCM region. Equations 2.1 through 2.8 follow Solomon's [6] analysis except for changes due to geometry.

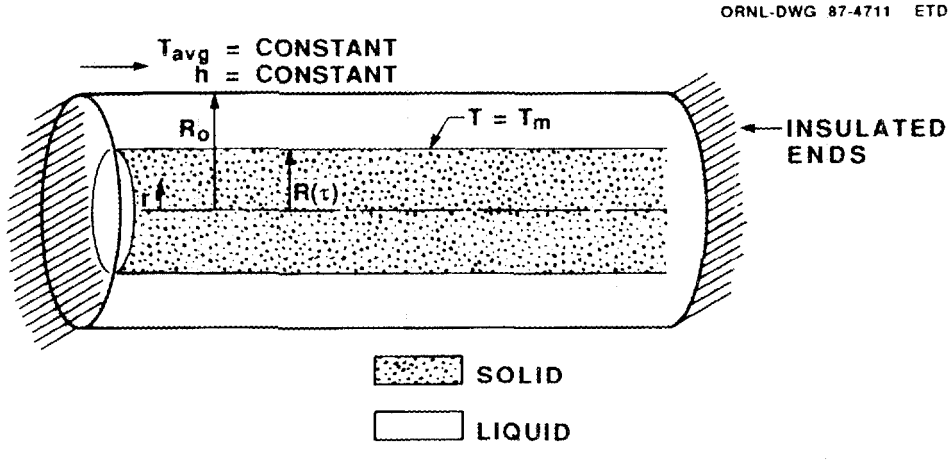

Fig. 2.1. Approximate Model of the PCM Region.

The temperature, $T(r,\tau)$, in the liquid region satisfies the heat equation, 2.1.

$$\frac{\partial T}{\partial \tau} = \frac{\alpha}{r}\frac{\partial}{\partial r}\left(r\,\frac{\partial T}{\partial r}\right) \qquad \text{for } r > R(\tau) \qquad \text{(Eq. 2.1)}$$

At the solid-liquid interface, the temperature equals the melting temperature and the rate of heat melting the solid PCM (and therefore moving the front) equals the rate of heat passing through the front. Equation 2.3 is discontinuous at $R(\tau) = 0$ because at this point the front ceases to exist.

$$T(R(\tau),\ \tau) = T_m \qquad \text{(Eq. 2.2)}$$

$$\rho\, L_f \frac{\partial\, R(\tau)}{\partial \tau} = -k\,\frac{\partial T(R(\tau),\ \tau)}{\partial r} \qquad \text{for } R(\tau) > 0 \qquad \text{(Eq. 2.3)}$$

At the container wall the rate of heat transfer to the PCM equals the convective heat transfer from the liquid metal. The heat capacity of the wall is assumed to be negligible here and is discussed further in Sect. 3.3.2.

$$-k\,\frac{\partial T(R_o,\ \tau)}{\partial r} = h(T(R_o,\ \tau) - T_{avg}) \qquad \text{(Eq. 2.4)}$$

For the quasi-steady approximation, Eq. 2.1 is replaced by the steady state equation (Eq. 2.5). It should be noted that the boundary conditions remain time dependent. This equation must be constrained to $R(\tau) > 0$ because the temperature of the center of the PCM is a function of time only (i.e., $\frac{\partial T(0,\tau)}{\partial r} = 0$) and the quasi-steady approximation fails at this point.

$$\frac{\partial}{\partial r}\left(r\,\frac{\partial T}{\partial r}\right) = 0 \qquad \text{for } r > R(\tau) > 0 \qquad \text{(Eq. 2.5)}$$

The solution to Eqs. 2.5 and 2.2 yields Eq. 2.6.

$$T(r, \tau) = T_m + a(\tau) \ln \frac{r}{R(\tau)} \qquad \text{for } r > R(\tau) > 0 \qquad \text{(Eq. 2.6)}$$

The variable, $a(\tau)$, is found by substituting this solution into Eq. 2.4 and is shown in Eq. 2.7.

$$a(\tau) = \frac{h(T_{avg} - T_m)}{\frac{k}{R_o} + h \ln \frac{R_o}{R(\tau)}} \qquad \text{for } R(\tau) > 0 \qquad \text{(Eq. 2.7)}$$

The flux equation at the interface, Eq. 2.3, can now be used with Eq. 2.6 (recognizing that as τ goes from 0 to τ, r goes from R_o to R) to solve for the position of the interface as given implicitly in Eq. 2.8.

$$\frac{-k\ h\ (T_{avg} - T_m)}{\rho\ L_f}\ \tau = \left\{\frac{k}{R_o} + h \ln R_o\right\}\left(\frac{R^2 - R_o^2}{2}\right) - h\left\{\frac{R^2 \ln R - R_o^2 \ln R_o}{2} - \frac{R^2 - R_o^2}{4}\right\} \qquad \text{for } R(\tau) > 0 \qquad \text{(Eq. 2.8)}$$

Up to this point, the approximate solution in the PCM region is very similar to that shown by Solomon [6]. From here onwards, the solution approach will be different to reflect the differences in both the problem geometry and the expected process application. When the PCM cylinder is completely melted, R is equal to zero (that is, the phase change front has moved to the center of the cylinder). However, this equation is discontinuous at R = 0. Therefore, to estimate the radius, R_o, for which the PCM cylinder is completely melted during the

test period, R is set equal to $R_o/100$ and τ is set to τ_d (test duration) in Eq. 2.8. Solving for R_o gives Eq. 2.9.

$$R_o \simeq \frac{-k}{h} \pm \sqrt{\left(\frac{k}{h}\right)^2 + \frac{4k}{\rho L_f} (T_{avg} - T_m) \tau_d} \qquad \text{(Eq. 2.9)}$$

This R_o is the radius that will yield the greatest storage density for the given set of simplified assumptions. For tubes with smaller radii, the melting is also complete within the test duration but more material could be melted. Therefore, for a cylinder of fixed wall thickness, the parasitic mass decreases with increasing radius and the storage density can increase with increasing radius. Above R_o, some of the PCM present will not melt and the storage density will decrease.

The heat transfer coefficient is not yet known and must be estimated before R_o can be calculated. This leads to the analysis of the liquid metal region and the coupling of the two regions.

2.2 Approximate Solution for the Liquid Metal Region

The approximate solution for the liquid metal region is sought to provide guidance in the selection of reasonable physical parameters for the finite difference solution. As discussed in the last section, an estimate for the convective heat transfer coefficient is required to estimate the PCM cylinder radius. Also, the outer radius of the liquid metal region annulus and the fluid velocity must be estimated to avoid exceeding the maximum permissible outlet temperature.

The flow of liquid metal in an annular region was examined by Dwyer [5, p. 78-79 and 10, p. 337-338] for a set of simplifying

assumptions. These assumptions include 1) heat transfer from the inner wall only, 2) uniform heat flux, 3) negligible axial heat conduction, and 4) fully developed velocity and temperature profiles. This problem was solved exactly for the laminar flow case and the results for average Nusselt number and bulk temperature are presented in tabular form (see Sect. 1.3) as a function of the ratio, R_f/R_o. These results were used in the form of Eqs. 2.10 and 2.11 for the computer program discussed in Sect. 2.3.

$$Nu = 0.78\ R_f/R_o + 4.6 \qquad \text{(Eq. 2.10)}$$

$$h = \frac{k\ Nu}{d_h} \qquad \text{(Eq. 2.11)}$$

The bulk liquid metal temperature is then a function of only the wall temperature, the thermal flux, and the radius ratio, R_f/R_o. The wall temperature at the outlet was assumed to equal the PCM melting temperature. The constant heat flux was taken equal to the required thermal load on the PCM tube, $\dot{q}$. This gives a constant liquid metal temperature for a constant wall temperature, T_m, as shown in Eq. 2.12.

$$T_{\ell m} = T_m + \dot{q}/(hA_{pout}) \qquad \text{(Eq. 2.12)}$$

2.3 Coupling the Liquid Metal and Phase Change Material Approximate Solutions

The PCM approximate model defined a maximum radius for which the PCM material would be completely melted during the test duration as a

function of the heat transfer coefficient, h. The liquid metal laminar flow solution defines the temperature and heat transfer coefficient as functions of the tube radius and the ratio of the adiabatic liquid metal radius to the tube radius. These two solutions are obviously tightly coupled.

Several constraints must be met by any coupled solution. The liquid metal flow and temperature change must meet, without exceeding greatly, the thermal load requirements (Eq. 2.13). The mass of the PCM and the liquid metal inventory must be capable of storing all the rejected heat over the test period duration (Eq. 2.14). The number of PCM tubes required should be as low as possible. The liquid metal velocity was constrained to values less than 5 m/s because higher flow velocities led to higher liquid metal exit temperatures.

$$\dot{m}\, c_p (T_{in} - T(z=L)) \geq \dot{W}_t \qquad \text{(Eq. 2.13)}$$

$$[\pi(R_f^2 - R_o^2)\, L\, (T_{out} - T_{init})\, c_p +$$

$$(\pi\, R_o^2\, L)\, (L_f + (T_m - T_{init})\, c_p)]\, (NPIPES) \geq \dot{W}_t\, \tau_d \qquad \text{(Eq. 2.14)}$$

These relationships and constraints were programmed into a small computer code that tested a wide range of variables to define feasible system parameters, listed in Table 2.1. The flow chart for this computer code is shown in Fig. 2.2.

Table 2.1. Preliminary System Parameters Based on Approximate Analysis

R_o (m)	R_f (m)	L (m)	v (m/s)	NPIPES
0.048	0.124	4.5	0.05	5000
0.049	0.136	4.5	0.04	4600
0.049	0.136	4.5	0.09	4600
0.048	0.124	5.0	0.10	4500
0.049	0.136	5.0	0.09	4100
0.044	0.124	5.0	0.05	5000
0.053	0.149	3.5	0.04	5000
0.053	0.149	3.5	0.08	5000
0.053	0.137	4.0	0.04	4700
0.053	0.137	4.0	0.09	4700
0.053	0.149	4.0	0.04	4300
0.053	0.149	4.0	0.08	4300
0.053	0.125	4.5	0.10	4600
0.053	0.137	4.5	0.09	4200
0.053	0.149	4.5	0.08	3900
0.053	0.125	5.0	0.10	4100
0.053	0.137	5.0	0.09	3800
0.053	0.149	5.0	0.08	3500
0.053	0.149	5.0	0.12	3500

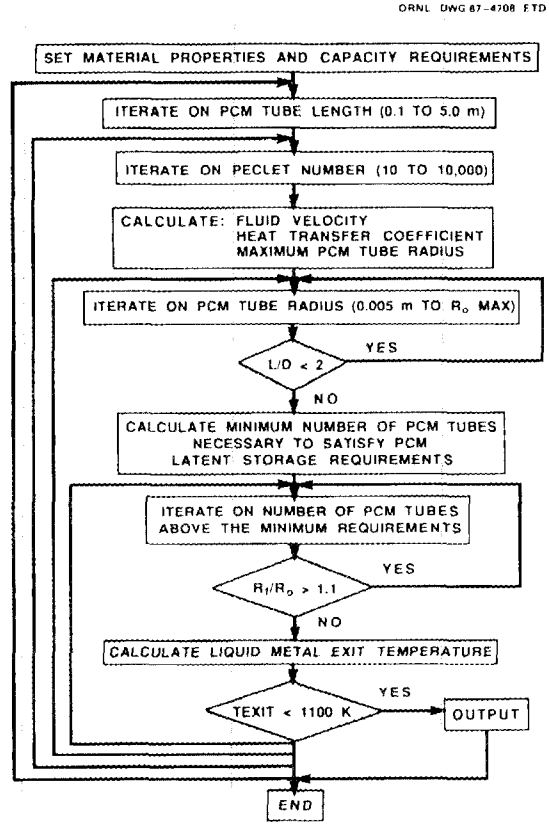

Fig. 2.2. Flow Chart for Approximate Solution Computer Code.

3. FINITE DIFFERENCE SOLUTION

3.1 Background

The approximate solutions included several simplifications that do not reflect the physical situation such as: 1) no axial variations, 2) uniform heat flux, 3) a quasi-steady state, 4) a constant inlet liquid metal temperature, and 5) an initial state of solid PCM at its melting temperature. An analytical approach to the overall problem would be too complex to allow an exact solution. Therefore, a numerical approach was used to model the behavior of a phase change storage system charged by a liquid-metal flow. Within the PCM region, this model is very similar to that used by Solomon, et al. [6]. However, the geometry, element definitions, and use pattern are different.

The PCM cylinder was assumed to be radially symmetric with insulated ends. The liquid metal flow has an artificial adiabatic external boundary as discussed in Sect. 1.2. The liquid metal is assumed to exchange heat only within the heat exchanger and with the thermal load source. That is, outside the PCM heat exchanger, the fluid travels in an insulated pipe so that there is no upstream or downstream conduction. An initial temperature for the system is specified.

An energy balance is performed for each element in the finite difference grid described in Sect. 3.2. The resulting equations are solved explicitly within the PCM region and implicitly within the

liquid metal region. Within the PCM region, the equations are identical to those used by Solomon, et al. [6] and are based on energy conservation, Fourier's law, and the equation of state, shown in Eqs. 3.1-3.3. The equation of state for constant specific heats for each phase is shown in Eq. 3.4 (where the internal energy, E, of the solid state PCM at its melting temperature has been set to zero).

$$\rho \frac{\partial E}{\partial \tau} + \nabla \cdot \bar{q} = 0 \qquad \text{(Eq. 3.1)}$$

$$\bar{q} = -k(T)\ \nabla T \qquad \text{(Eq. 3.2)}$$

$$C(T) = \frac{dE(T)}{dT} \qquad \text{(Eq. 3.3)}$$

$$T = \begin{cases} T_m + \dfrac{E}{c_s}\ , & E < 0 \text{ (solid phase)} \\ T_m\ , & 0 < E < L_f \text{ (melting zone)} \\ T_m + \dfrac{(E - L_f)}{c_\ell}\ , & E > L_f \text{ (liquid phase)} \end{cases} \qquad \text{(Eq. 3.4)}$$

A "Kirchoff" temperature, U, was defined by Solomon [6, p. 18] and is useful because the position of the phase change front becomes a part of the solution rather than an assumption that must be iterated upon within the calculations. Equations 3.5-3.10 outline these energy conservation equations in terms of this "Kirchoff" temperature (defined in Eq. 3.6).

$$K(T) = \begin{cases} k_s\ , & T < T_m \\ k_L\ , & T > T_m \end{cases} \qquad \text{(Eq. 3.5)}$$

$$U = \int_{T_m}^{T} K(s)ds = \begin{cases} k_s\ (T - T_m)\ , & T < T_m \\ 0\ , & T = T_m \\ k_\ell\ (T - T_m)\ , & T > T_m \end{cases} \qquad \text{(Eq. 3.6)}$$

$$\nabla U = K(T)\nabla T \qquad \text{(Eq. 3.7)}$$

$$\overline{q} = -\nabla U \qquad \text{(Eq. 3.8)}$$

$$\rho \frac{\partial E}{\partial \tau} = \nabla \cdot (\nabla U) \qquad \text{(Eq. 3.9)}$$

$$U = \begin{cases} \dfrac{k_s\ E}{c_s}\ , & E < 0 \\ 0\ , & 0 < E < L_f \\ \dfrac{k_\ell\ (E - L_f)}{c_\ell}\ , & E > L_f \end{cases} \qquad \text{(Eq. 3.10)}$$

This Kirchoff temperature approach used by Solomon is very similar to the enthalpy model discussed by Shamsundar and Sparrow [7]. They rigorously verified the enthalpy model and defined a dimensionless enthalpy, θ, as shown in Eq. 3.11. The dimensionless time parameter is the Fourier number, Fo, Eq. 3.12. Shamsunder and Sparrow used the dimensionless product, FoSte as a dimensionless time parameter because it correlates the results for various values of Ste, defined in Eq. 3.13. The enhanced PCM mixtures discussed in Chap. 4 represent a range of Stefan numbers, so this product has been used in the presentation of results.

$$\theta = \frac{1}{\rho V} \int_V \rho \frac{(i - i_s^*)}{L_f}\, dV \qquad \text{(Eq. 3.11)}$$

$$Fo = \alpha\tau/R_o^2 \qquad \text{(Eq. 3.12)}$$

$$Ste = c_s\,(T_m - T_{init})/L_f \qquad \text{(Eq. 3.13)}$$

For a material with an assumed constant density and a constant latent heat, and because the internal energy variable, E, was defined equal to zero at the solid state melting temperature, Eq. 3.11 can be rewritten as Eq. 3.14. In this equation, θ describes the energy content of the PCM relative to the latent storage capacity and relative to the energy content at the solid state melting temperature. A dimensionless measure of the energy storage in the PCM can be constructed by taking the difference between the value of θ at a given point in time and the initial value of θ, see Eq. 3.15. The dimensionless temperature, ϕ, is defined in Eq. 3.16. The results will be presented in terms of these dimensionless variables for generality.

$$\theta = \frac{1}{VL_f}\int_V E\,dV = \frac{1}{VL_f}\sum_{1,1}^{M,N} E_{ij}V_{ij} \qquad \text{(Eq. 3.14)}$$

$$\theta^* = \theta - \theta_{initial} \qquad \text{(Eq. 3.15)}$$

$$\phi = \frac{T - T_{init}}{T_m - T_{init}} \qquad \text{(Eq. 3.16)}$$

Within the liquid metal region, no phase change occurs. Hence, the Kirchoff temperature offers no advantage and the internal energy is calculated implicitly. The liquid metal calculations were originally done in an explicit manner similar to those in the PCM region. However, the liquid metal has a much higher conductivity than the PCM and required a very small time step to avoid stability problems (see Sect. 3.3.1). This, in turn, caused the computer program to

consume excessive CPU time for each test case. This portion of the code was therefore rewritten using an implicit solution method for tridiagonal matrices outlined in Forsythe and Wasow [18, p. 104].

3.2 Finite Difference Grid Definition and Solution

The problem was defined in two spatial coordinates, r and z, and one temporal coordinate, τ. Although each node represents a small, thin, cylindrical volume, the finite difference formulation is rectangular in nature. The grid used is shown in Fig. 3.1. The areas and volumes of these grid elements are shown in Table 3.1. In this table, "i" is used to denote the node index in the r-direction and "j" is used for the z-direction. A single r-direction grid node is used for the liquid metal region because this is sufficient to determine the bulk fluid temperature as a function of z and τ. This bulk fluid

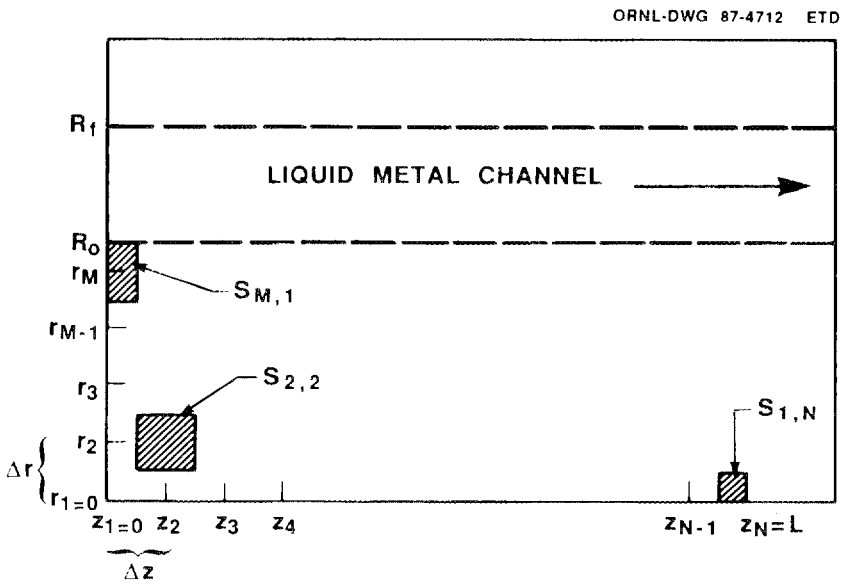

Fig. 3.1. Finite Difference Element Grid.

Table 3.1. Finite Difference Areas and Volumes

i	j	Cross-sectional area[a]	Inner perimeter area[b]	Outer perimeter area[c]	Volume
1	1	$\pi\ \Delta r^2/4$	0	$\pi\Delta r\Delta z/2$	$\pi\left(\frac{\Delta r}{2}\right)^2 \frac{\Delta z}{2}$
1	2-(N-1)	$\pi\ \Delta r^2/4$	0	$\pi\Delta r\Delta z$	$\pi\left(\frac{\Delta r}{2}\right)^2 \Delta z$
1	N	$\pi\ \Delta r^2/4$	0	$\pi\Delta r\Delta z/2$	$\pi\left(\frac{\Delta r}{2}\right)^2 \frac{\Delta z}{2}$
2-M	1	$2\pi r_i \Delta r$	$\pi\ r_i - \frac{\Delta r}{2} \Delta z$	$\pi\ r_i + \frac{\Delta r}{2} \Delta z$	$\pi r_i \Delta r \Delta z$
2-M	2-(N-1)	$2\pi r_i \Delta r$	$2\pi\ r_i - \frac{\Delta r}{2} \Delta z$	$2\pi\ r_i + \frac{\Delta r}{2} \Delta z$	$2\pi r_i \Delta r \Delta z$
2-M	N	$2\pi r_i \Delta r$	$\pi\ r_i - \frac{\Delta r}{2} \Delta z$	$\pi\ r_i + \frac{\Delta r}{2} \Delta z$	$\pi r_i \Delta r \Delta z$
M+1[d]	1	$\pi(R_f^2 - R_o^2)$	$2\pi R_o \frac{\Delta z}{2}$	0[e]	$\pi(R_f^2 - R_o^2) \frac{\Delta z}{2}$
M+1	2-(N-1)	$\pi(R_f^2 - R_o^2)$	$2\pi R_o \Delta z$	0	$\pi(R_f^2 - R_o^2) \Delta z$
M+1	N	$\pi(R_f^2 - R_o^2)$	$2\pi R_o \frac{\Delta z}{2}$	0	$\pi(R_f^2 - R_o^2) \frac{\Delta z}{2}$

[a] Area of element face perpendicular to the Z-axis.

[b] Area of element face parallel to the Z-axis and closest to the center of the cylinder.

[c] Area of element face parallel to the Z-axis and farthest from the center of the cylinder.

[d] "M+1" represents the node in the liquid metal region.

[e] Area taken as zero because this is an adiabatic surface.

temperature, in turn, is sufficient to determine the heat transfer to the PCM cylinder nodes and to test for the maximum allowable liquid metal exit temperature.

The internal energy, temperature, and Kirchoff temperature of each node are taken to represent both the point values and the mean values for each node at each point in time.

A PCM node is shown in Fig. 3.2. The general form of the energy balance is shown in Eq. 3.17, where the volumes and areas are defined in Table 3.1. The superscript of "n+1" indicates the value at the next point in time. Values without superscripts indicate the value at the current point in time. The updated value is explicitly calculated based on the values for the current point in time. The use of this general form equation is defined in Table 3.2 where q_1, q_2, q_3, and q_4 are defined in terms of q_a, q_b, q_c, q_d, and q_e (defined in Eqs. 3.18-3.22) for all nodes within the PCM region. Equation 3.23 demonstrates the use of the general form (Eq. 3.17) and Table 3.2 for

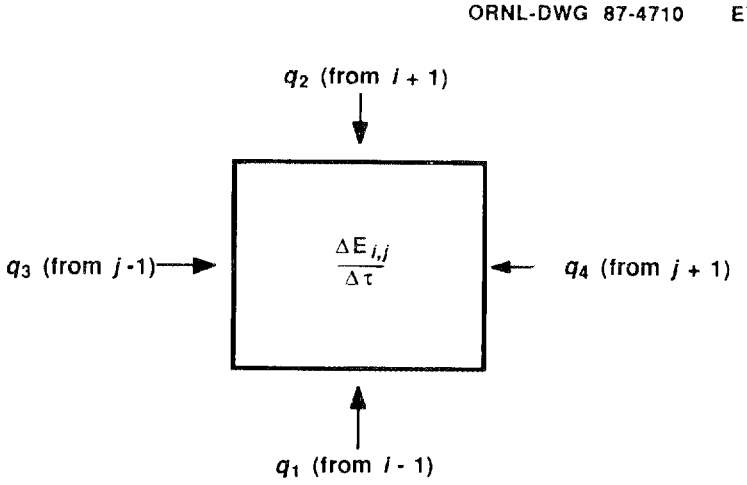

Fig. 3.2. PCM Node Energy Balance.

Table 3.2. Application of Energy Balance Equation for Each Finite Difference Node

i	j	q_1	q_2	q_3	q_4
1	1	0	q_b	0	q_d
1	2-(N-1)	0	q_b	q_c	q_d
1	N	0	q_b	q_c	0
2-(M-1)	1	q_a	q_b	0	q_d
2-(M-1)	2-(N-1)	q_a	q_b	q_c	q_d
2-(M-1)	N	q_a	q_b	q_c	0
M	1	q_a	q_e	0	q_d
M	2-(N-1)	q_a	q_e	q_c	q_d
M	N	q_a	q_e	q_c	0

the internal PCM region ($1 < i < M$, $1 < j < N$).

$$\rho V_{ij} \left(\frac{E_{ij}^{n+1} - E_{ij}}{\Delta\tau} \right) = q_1 + q_2 + q_3 + q_4 \qquad \text{(Eq. 3.17)}$$

$$q_a = \frac{A_{pin_{ij}}}{\Delta r} (U_{i-1,j} - U_{ij}) \qquad \text{(Eq. 3.18)}$$

$$q_b = \frac{A_{poutij}}{\Delta r} (U_{i+1,j} - U_{ij}) \qquad \text{(Eq. 3.19)}$$

$$q_c = \frac{A_{cij}}{\Delta z} (U_{i,j-1} - U_{ij}) \qquad \text{(Eq. 3.20)}$$

$$q_d = \frac{A_{cij}}{\Delta z} (U_{i,j+1} - U_{ij}) \qquad \text{(Eq. 3.21)}$$

$$q_e = h\, A_{poutij} (T_{m+1,j} - T_{mj}) \qquad \text{(Eq. 3.22)}$$

$$\rho V_{ij} \frac{E_{ij}^{n+1} - E_{ij}}{\Delta\tau} = \frac{A_{pin_{ij}}}{\Delta r} (U_{i-1,j} - U_{ij}) + \frac{A_{pout_{ij}}}{\Delta r} (U_{i+1,j} - U_{ij}) + \frac{A_c}{\Delta z} (U_{i,j-1} - U_{ij}) + \frac{A_c}{\Delta z} (U_{i,j+1} - U_{ij}) \quad \text{(Eq. 3.23)}$$

The liquid metal region is solved implicitly using Eq. 3.24 (for $1 < j < N$) and 3.25 (for $j=N$). The areas and volumes for these equations were shown in Table 3.1. After this matrix of equations is solved, the liquid metal inlet temperature is calculated using Eq. 3.26.

$$0 = \frac{\rho V_{M+1,j}}{\Delta\tau} E_{M+1,j} + hA_{pin_{M+1,j}} (-T_M + T_{M,j}^{n+1}) + E_{M+1,j-1}^{n+1} \left(\frac{A_{c_{M+1,j}}}{\Delta z} \frac{k}{c_p} + \rho v \frac{A_{c_{M+1,j}}}{2} \right) + E_{M+1,j}^{n+1} \left(-\frac{\rho V_{M+1,j}}{\Delta\tau} - \frac{h A_{pin_{M+1,j}}}{c_o} - \frac{2 A_{c_{M+1,j}}}{\Delta z} \frac{k}{c_p} \right) + E_{M+1,j}^{n+1} \left(\frac{A_{c_{M+1,j}}}{\Delta z} - \rho v \frac{A_c}{2} \right) \quad \text{(Eq. 3.24)}$$

$$0 = \frac{\rho V_{M+1,N}}{\Delta\tau} E_{M+1,N} + hA_{pin_{M+1,N}} \left(-T_M + T_{M+1,N}^{n+1} \right) + E_{M+1,N-1}^{n+1} \left(\frac{A_{c_{M+1,N}}}{\Delta z} \frac{k}{c_p} + \frac{\rho V A_{c_{M+1,N}}}{2} \right) + E_{M+1,N}^{n+1} \left(-\rho \frac{V_{M+1,N}}{\Delta\tau} - \frac{h A_{pin_{M+1,N}}}{c_p} - \frac{A_{c_{M+1,N}}}{\Delta z} \frac{k}{c_p} - \frac{\rho v A_{c_{M+1,N}}}{2} \right) \quad \text{(Eq. 3.25)}$$

$$T^{n+1}(M+1,1) = T\ (M+1,N) + \frac{\dot{w}}{\dot{m}cp} \qquad \text{(Eq. 3.26)}$$

The heat transfer coefficient between the liquid metal flow and the PCM is calculated conservatively (the value is actually greater in the thermal and hydraulic development length) using Eq. 3.27 [11]. This and other correlations available for liquid metal annular flow cases were discussed in Sect. 1.3.

$$Nu = (6.15 + 0.02\ Pe^{0.8}) \qquad \text{(Eq. 3.27)}$$

3.3 Computer Code Considerations

3.3.1 Computer code stability

Several factors must be considered when designing and using a finite-difference computer code. The time-step size is the most crucial of these factors. The time step must be smaller than the smallest time "response" of any element in the model as defined in Eq. 3.28 from Dusinberre [8, p. 13]. Equations 3.29, 3.30, and 3.31 show this response time for an external (closest to the liquid metal flow) PCM element, an element at the center of the PCM tube, and a liquid metal region element, respectively.

$$\Delta\tau \leq \frac{V\rho}{\Sigma\ \frac{kA}{\Delta L}} \qquad \text{(Eq. 3.28)}$$

$$\Delta\tau \leq \frac{c_p\ V_{i,j}\rho}{\left(h\ A_{pout_{ij}} + \frac{kA_{pin_{ij}}}{\Delta r} + \frac{2\ A_{c_{ij}}\ k}{\Delta z} \right)} \qquad \text{(Eq. 3.29)}$$

$$\Delta\tau \leq \frac{c_p V_{ij}\rho}{\left(\frac{k\ A_{pout_{ij}}}{\Delta r} + \frac{2\ A_{c_{ij}}\ k}{\Delta z} \right)} \qquad \text{(Eq. 3.30)}$$

$$\Delta\tau \leq \frac{c_p V_{ij} \rho}{\left(h A_{pin_{ij}} + \frac{\rho V c_p A_{c_{ij}}}{2} + \frac{2 A_{c_{ijk}}}{\Delta z} \right)} \qquad \text{(Eq. 3.31)}$$

Due to the higher conductivity of the liquid metal, the time step size for this region was always several orders of magnitude smaller than that needed for the PCM region. This portion of the code was therefore rewritten in an implicit manner. The stability of the implicit formulation is not as easily defined as that of the explicit formulation. The implicit approach is expected to be stable at very large time steps but the only way to test the stability is to vary the time-step size and examine the effect on the results. Therefore, the code was run with six radial subdividions and a variety of time-step sizes. The maximum time-step size for this examination was set by the requirements of the explicit portion of the code. The results of this test are shown in Fig. 3.3 in the form of the liquid metal temperature profile after 100 s. These consistent shape of these curves indicates that the solution is indeed stable for the time step sizes under consideration. The accuracy of the liquid metal exit temperature is acceptable considering other approximations used in the finite-difference model.

Radial and axial step sizes were examined in a similar manner. The number of radial subdivisions was varied from 3 to 24. The axial step size was automatically adjusted so that the perimeter and cross-sectional area for a PCM element were of the same order of magnitude. The finite difference code automatically stops when the liquid

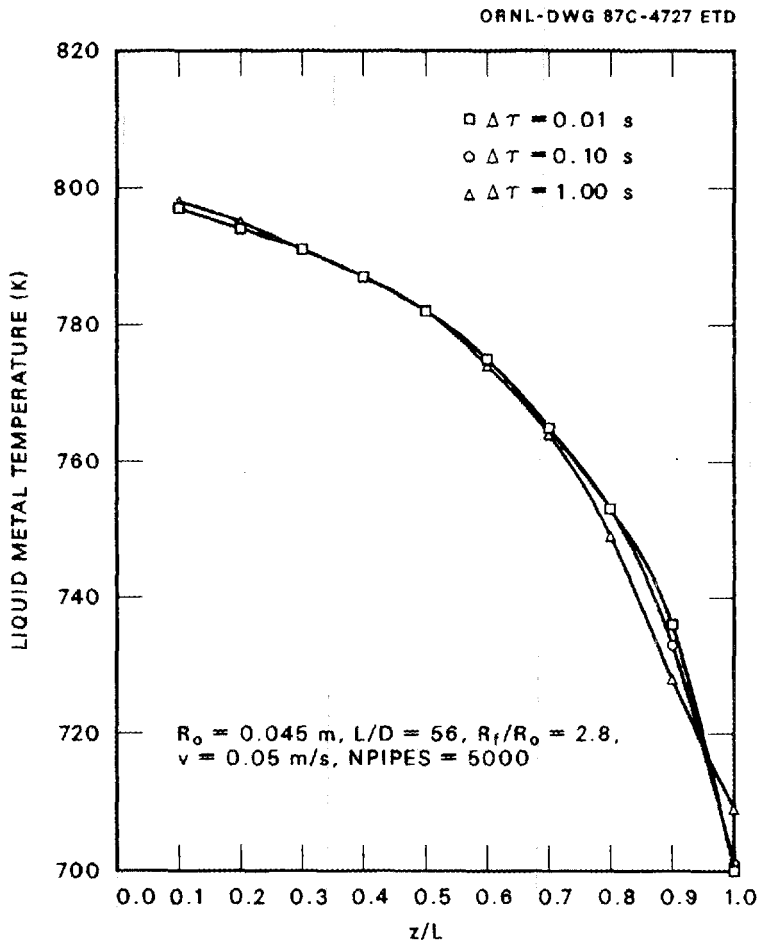

Fig. 3.3. Influence of Time-Step Size on the Stability of the Implicit Solution.

metal exit temperature exceeds 1100°K. The time at which this condition was met was very sensitive to the number of radial subdivisions, varying from 964 seconds at 3 subdivisions down to 697 seconds at 24 subdivisions. The results shown in Figs. 3.4 and 3.5 reflect the PCM condition at the stopping point determined by the liquid metal exit temperature limit.

Figure 3.4 shows the effect of element size on the dimensionless PCM temperature at the outer surface of the tube and in the center of the tube. The outer surface temperature is relatively unaffected by

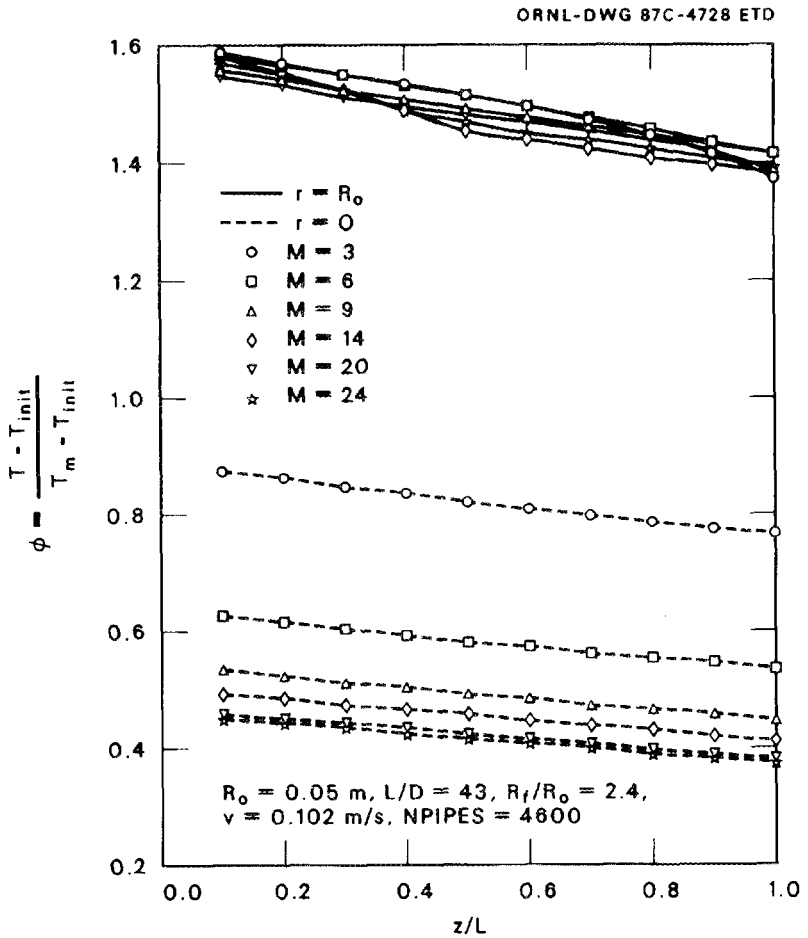

Fig. 3.4. Effect of Element Size on PCM Dimensionless Temperature Profile.

the number of divisions but the temperature at the center of the tube is strongly affected. Figure 3.5 shows the effect of element size on θ*, the dimensionless energy storage of the tube and the Fourier number corresponding to the time at which the liquid metal exit temperature exceeds 1100°K. Based on an examination of these figures, nine subdivisions were used for all subsequent tests. This is a compromise between accuracy and efficiency. The computer code running time increases at a rate roughly proportional to the number of radial divisions, from 14 Cray CPU minutes for M = 3 to 126 Cray CPU minutes

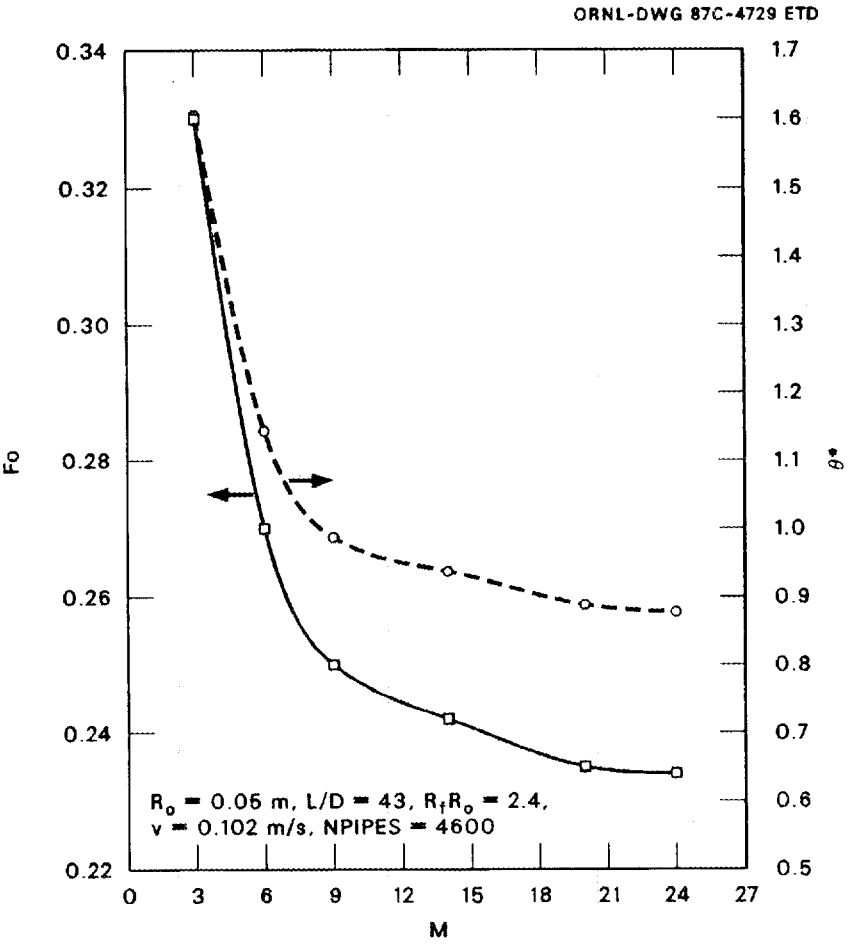

Fig. 3.5. Effect of Element Size on Test Duration (F_o) and Energy Storage (θ^*).

for M = 24. At nine subdivisions, the predicted energy storage is within 13% and time value is within 10% of the more accurate tests. This accuracy is therefore considered acceptable considering the wide range of potential design parameters discussed in Sect. 1.2. The final computer runs for the enhanced configurations used from 53 to 153 CPU minutes on the Cray computer.

3.3.2 Computer code development

The overall computer code flow chart is shown in Fig. 3.6. This figure and the results presented in this report reflect the final form of the computer code. However, several subjects explored during the development of this code are worth discussing. The change from an explicit to an implicit treatment of the liquid metal region has already been discussed. Another important facet of the development included the addition, and ultimately the deletion, of a segment of the code that modeled the PCM containment tube wall.

The inclusion of the tube wall complicated the code in several ways. The code was found to be better-behaved if the cross-sectional areas of each finite difference node were of the same order of magnitude as the axial areas. Because the tube wall was so much thinner than the PCM region, achieving such a balance was very difficult. Additionally, at the juncture of the PCM and the wall, it was necessary to know the PCM's conductivity, which in turn required knowledge of the phase at that point in space and time. This somewhat nullified the advantages inherent in the Kirchoff temperature approach. Additionally, the tube wall's high conductivity and small physical dimensions led to very small time steps, on the order of those required for the liquid metal region. Moreover, after going through all these correction procedures to the extent possible, the temperature difference across the tube wall was always much smaller than the difference between the liquid metal and PCM temperatures.

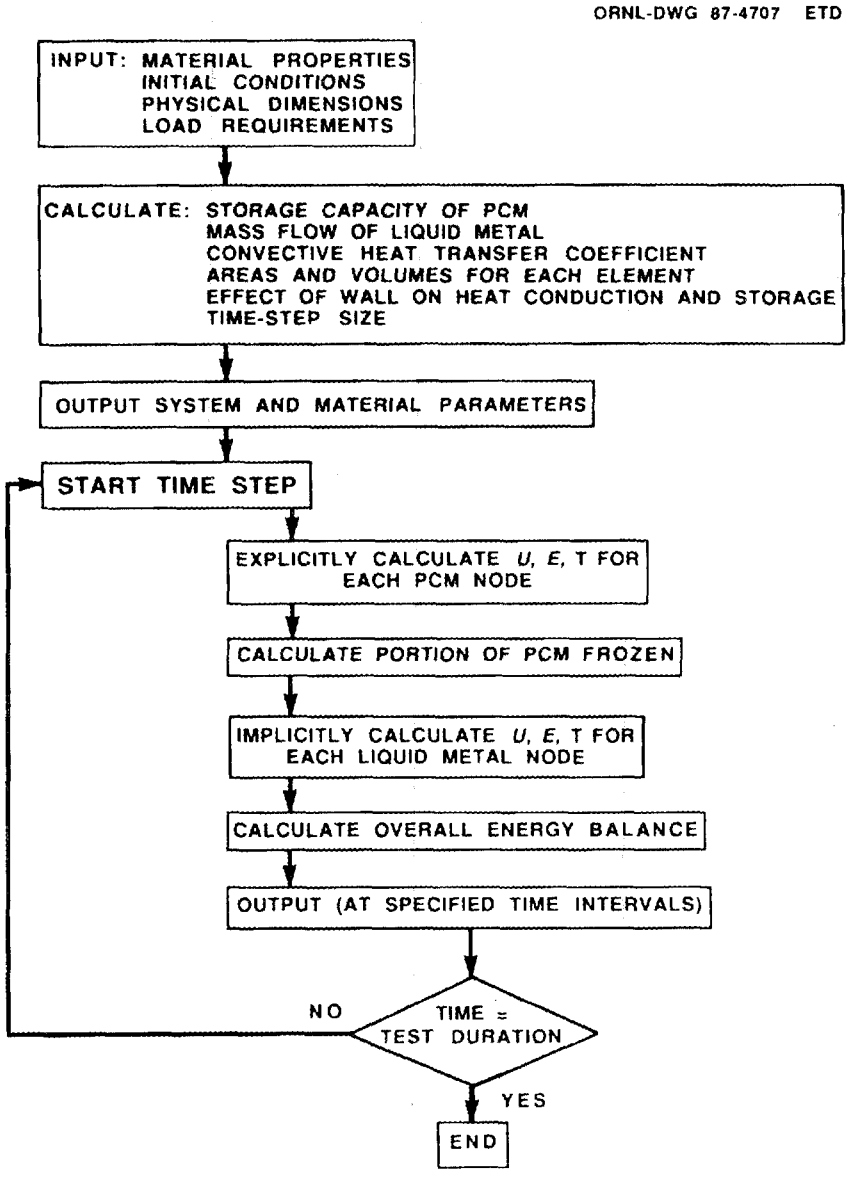

Fig. 3.6. Flow Chart for Finite Difference Computer Code.

After deciding to remove the tube wall portion of the model from the code, several caveats were added to the code. The code now calculates the thermal storage capacity of the tube wall and compares it to the thermal storage capacity of the PCM. This value is printed out and an excessively large value will stop the code's execution. Also,

the convective heat transfer coefficient is compared to the overall heat transfer coefficient (Eq. 3.32) including the wall. This value is also printed out and can stop the code's execution. These precautions will be of value if other tube wall thicknesses or materials are examined at a future time.

$$h_{overall} = \frac{1}{\frac{1}{h} + \frac{t_w}{k_w}} \qquad \text{(Eq. 3.32)}$$

3.4 Enhanced Configurations

As will be demonstrated in Sects. 4.1 and 4.2, the limiting factor of the PCM energy storage system is the poor conductivity of the PCM material. This conductivity, as was shown in Table 1.1, is about one-tenth the conductivity of either the liquid metal or the tube wall. If the PCM conductivity were higher, the tube radius could be larger, the number of tubes could be smaller, and the liquid metal flow rate could likely be lower.

Three enhancement methods are considered in this study. They involve replacing some portion, measured as a volume percent, of the PCM with: 1) a reticulated metal insert, 2) thin fins, or 3) liquid lithium (to make a metal salt/molten metal slurry). A mixed enthalpy approach is used to model these enhancements with the finite difference code.

The mixed enthalpy approach is based on an assumption that the enhanced PCM mixture behaves as a homogenous material. Knowles and Webb [9] have defined optimum fin dispersion requirements for which

this assumption is rigorously true. These dispersion requirements are based on two conditions: 1) the fins must be perpendicular to the heat transfer face and 2) the fins must be thin enough that the thermal resistance along the fins must be greater than the resistance across the PCM layers. For cylindrical geometries, this means that the enhancement material should be arranged perpendicular to the outer face of the cylinder and the concentration should be inversely proportional to the radius. The applicability of this approach for thin fins has been experimentally confirmed by Knowles and Webb [9].

The mixed enthalpy method is implemented by calculating new "mixed" values for the density, heat capacity, conductivity, and latent heat of the PCM mixture (see Eqs. 3.33-3.36). In Eq. 3.34, the specific heat of each material is first converted to a volumetric specific heat (used and empirically documented by Knowles and Webb [9]), weighted according the volumetric fraction of the addition material, and finally reconverted to a mass basis using the density of the mixture. The latent heat of the mixture (Eq. 3.36) must reflect not only the fact that a portion of the material does not undergo a phase change, but also the new, greater density of the mixture.

$$\rho_{mix} = x\,\rho_{add} + (1 - x)\,\rho_{pcm} \qquad \text{(Eq. 3.33)}$$

$$c_{p\ mix} = \frac{x c_{p_{add}} \rho_{add} + (1 - x)\, c_{p_{pcm}} \rho_{pcm}}{\rho_{mix}} \qquad \text{(Eq. 3.34)}$$

$$k_{mix} = x\,k_{add} + (1 - x)\,k_{pcm} \qquad \text{(Eq. 3.35)}$$

$$L_{fmix} = \frac{\rho_{pcm}}{\rho_{mix}} (1 - x)\, L_{f_{pcm}} \qquad \text{(Eq. 3.36)}$$

Both aluminum and nickel are available as a reticulated material (similar to steel wool) with void fractions from 90 to 95%. Aluminum has a much higher conductivity but unfortunately a melting point below the application under consideration. Nickel was therefore chosen as the material for the reticulated metal insert and its properties are shown in Table 3.3. Both 90 and 95% void fractions were modeled.

Table 3.3. Enhancement Material Properties

	Nickel[a]
k	55.0 W/m-°K
c_p	0.444 J/g-°K
ρ	8.906×10^6 g/m^3
	Liquid Lithium[b]
k	12.22 W/m-°K
c_p	4.6 J/g-°K
ρ	4.65×10^5 g/m^3

[a] c_p and ρ at 20°C, k at 600°K [3].
[b] at 973°K [14].

The fins were made out of the same material as the tube wall, 304SS. The properties for this material were listed in Table 1.1. Fin volume fractions from 5 to 50% were modeled.

The metal/metal-salt mixture is generated by adding liquid lithium to the lithium hydride salt. This addition not only enhances the heat transfer but is also valuable because it significantly reduces the PCM's hydrogen pressure as can be seen in Fig. 3.7. This reduction, in turn, simplifies the PCM containment problem. Volume fractions of liquid lithium from 10 to 50% were modeled.

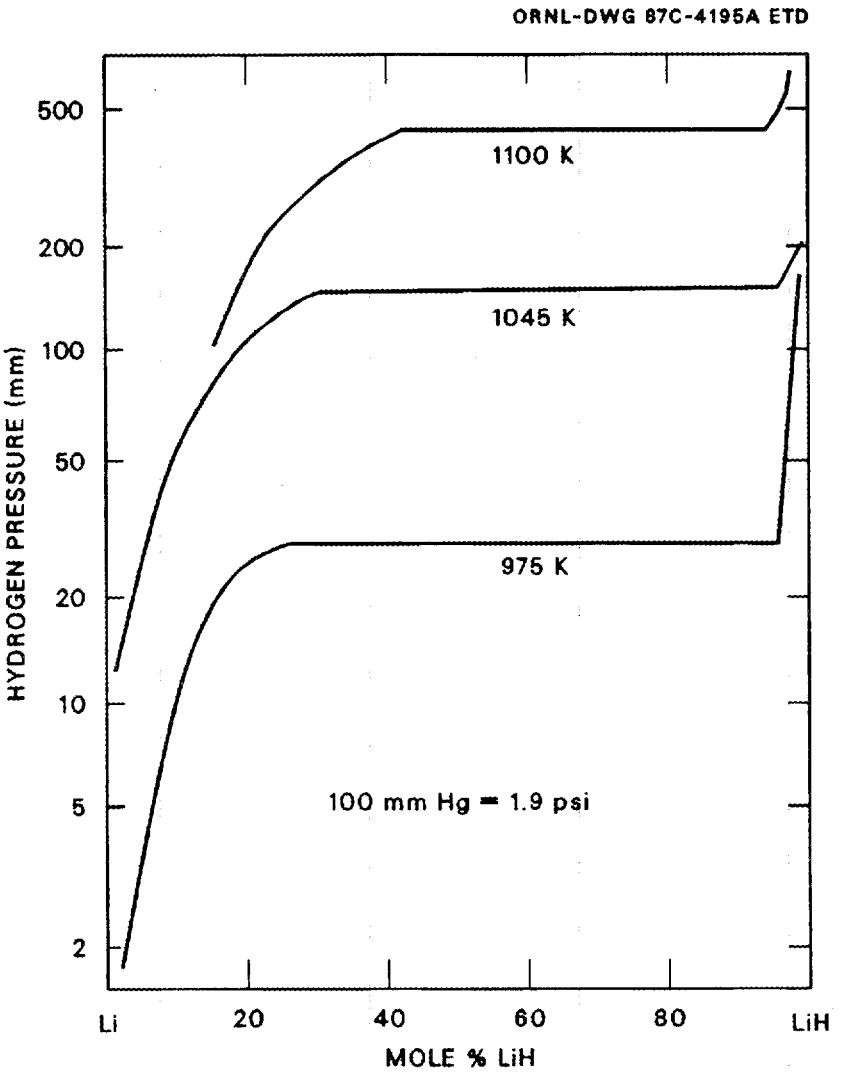

Fig. 3.7. LiH Hydrogen Pressure is Lowered by the Addition of Liquid Lithium.

4. RESULTS

4.1 Unenhanced System Configurations

Initial system configuration estimates were based on the results of the approximate analysis described in Chap. 2. An initial screening of the candidate systems reported in Table 2.1 was made with only three radial subdivisions to save computer time. Only one of these configurations was able to satisfy the thermal load for the target test duration of 1000 seconds. This configuration was the one with the smallest value of R_o and an R_f/R_o ratio of 3. Therefore, another set of trial cases was generated with still smaller tube radii, recognizing that as the number of radial subdivisions was raised to nine (see Sect. 3.3.1 for a discussion of accuracy requirements), the thermal load would be satisfied for a still shorter period of time. This second set of cases is shown in Table 4.1. The number of tubes required for these estimates was based on the thermal storage capacity of both the PCM and the liquid metal within the annular region.

All of these trial configurations were able to satisfy the thermal storage demand for the target operating period of 900 to 1000 seconds. However, the system energy density was low and only a small portion of the PCM was melted. Therefore, for two configurations, the number of tubes was then reduced below the estimated requirements to increase the energy storage load on each tube. This increased both the energy storage density and the proportion of energy stored in the form of latent heat, as is shown in Fig. 4.1. For two of these tube configurations, the liquid metal exit temperature exceeded the allowable exit temperature at operating periods of 900 to

Table 4.1. System Configurations[a] Based on Finite Difference Analysis

R_o	L/D	Number of PCM tubes	Ratio of latent to sensible storage in PCM	θ*	PCM[b] energy storage (10^6 J/tube)	System energy storage (10^6 J/tube)	System[c] energy density (J/g)
0.01	175	247,000	0.021	0.755	1.30	3.04	414
0.03	58	27,000	0.015	0.698	10.8	27.2	421
	67	24,000	0.019	0.698	12.3	31.1	421
	83	19,000	0.029	0.698	15.5	39.0	421
0.05	35	10,000	0.024	0.608	25.9	75.5	422
	35	5,700[d,e]	0.400	1.05	45.1	119	663
	40	9,000	0.028	0.608	29.7	86.4	422
	50	7,000	0.036	0.608	37.4	108	423
	50	5,000[d]	0.347	0.954	58.7	149	584
	50	4,000[d,f]	0.434	1.11	68.0	177	691

[a] Liquid metal velocity = 0.04 m/s, R_f/R_o = 3.

[b] Includes PCM only, not tube wall or liquid metal.

[c] System includes tube wall and liquid metal in annular region.

[d] Number of tubes reduced to increase thermal load on each tube.

[e] For this case, τ_d = 907 seconds.

[f] For this case τ_d = 947 seconds.

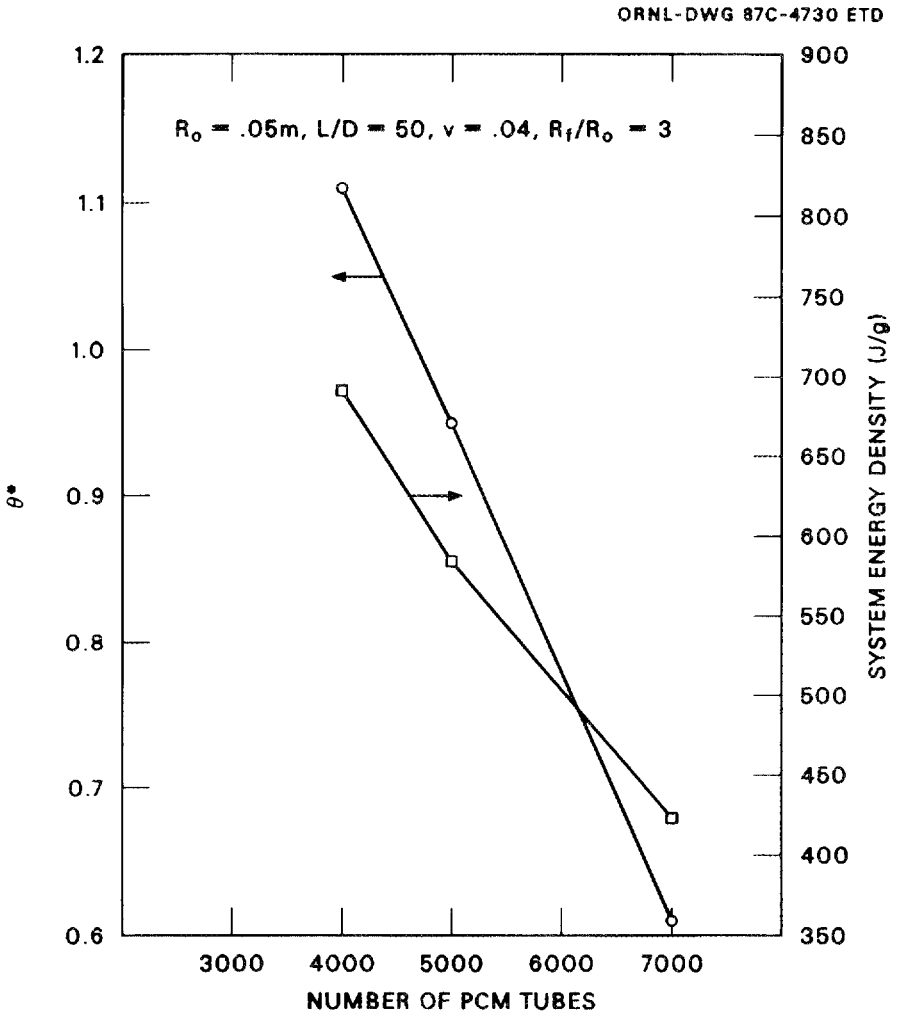

Fig. 4.1. Energy Stored per Tube vs Number of PCM tubes.

950 seconds, as noted on the table. The maximum operational period is therefore, an important factor in defining the maximum energy storage density attainable. The last configuration listed on Table 4.1 was chosen as a basis of comparison for the enhanced configurations in Sect. 4.2. It is important to note, however, that this configuration does not represent an optimum, as is discussed below.

The length to diameter ratio had no effect on the energy storage density for these configurations because of the way the required number of tubes was estimated. An increase in this ratio increases the

proportion of energy stored as latent heat for those cases with a lower energy storage density. However, for the cases where the thermal load per tube is increased, the length to diameter ratio has almost no effect on the proportion of latent energy stored. This parameter is apparently important only for those cases where the thermal load is so small that the melting front remains very close to the surface of the PCM tube throughout the test period.

The high (about 60%) proportion of sensible heat storage in the PCM is largely attributable to the difference between the initial system temperature of 700°K and the PCM melt temperature of 962°K.

The amount of energy stored in the increased internal energy of the liquid metal heat transfer fluid was very high, about 1.5 times the amount of energy stored in the PCM tube. This can be seen in Table 4.1 where the system energy storage and system energy density include the liquid metal inventory within the annular region. Considering this ineffective distribution of energy storage, several other configurations were tested, with smaller radii and with smaller R_f/R_o ratios. Most of these cases were unable to satisfy the operating period requirements. However, one test case did satisfy this requirement and shows that the system configurations discussed above are far from optimum. This case was identical to the fourth case listed in Table 4.1 except that the R_f/R_o ratio was decreased to 2.0. The ratio of latent to sensible energy storage in the PCM tube increased from 0.029 to 0.504, θ^* increased from 0.698 to 1.246, the system energy density increased from 421 to 973 J/g, and the ratio of energy

stored in the liquid metal to that stored in the PCM dropped from 1.5 to 0.41.

Based on this example, and on the large number of system parameters that could be varied, the system performance reported in this study should be used only to measure the relative value of system enhancements, not as an absolute measure of potential system performance.

4.2 Enhanced System Comparisons

The three enhancement options were described in Sect. 3.4 and include the insertion of a reticulated nickel material, the addition of thin fins, and the addition of liquid lithium to the PCM. These enhancements had a modest effect on system performance, increasing both the length of time for which the thermal load could be met and the total energy stored. The decrease in energy storage density varies greatly among the enhancement options. The following comparisons are based on a maximum operating period of 1000 seconds, as described in the problem definition in Sect. 1.2. Section 4.3 will describe some alternative bases for comparison.

The operational period of the unenhanced system was 947 seconds. The addition of thin fins and the insertion of reticulated nickel material increased the operational period beyond 1000 seconds. The addition of liquid lithium increased the operational period to 960 seconds for a 10% addition; however, the operational time for larger additions was decreased. Figure 4.2 summarizes the effect of these enhancement options on the operating period.

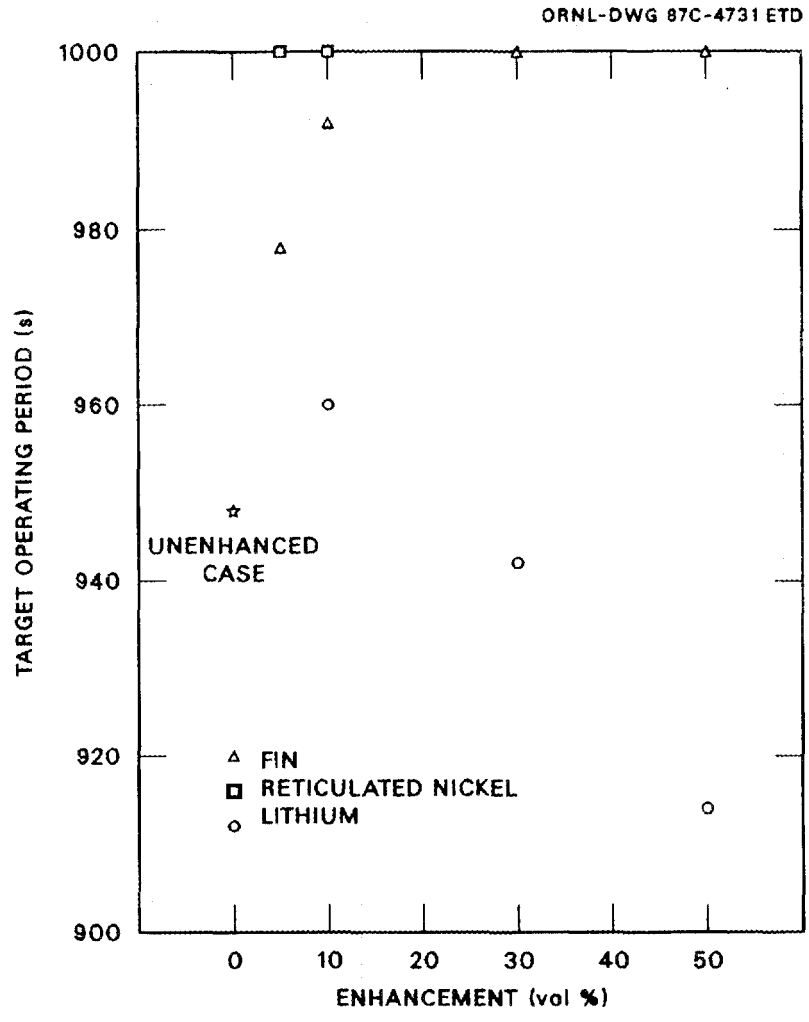

Fig. 4.2. Effect of Enhancements on Test Durations.

The amount of energy stored was increased by up to 6% by the use of a reticulated nickel insert or by the addition of thin fins, as seen in Fig. 4.3. The energy storage benefits of the 90 and 95% void fraction nickel inserts are the same. Two thirds of the energy storage increase attainable by the addition of thin fins is available at only a 10% volume addition. The energy storage doesn't increase at all when the volume fraction of the fin material is increased further from 30 to 50%. The addition of liquid lithium increased the energy

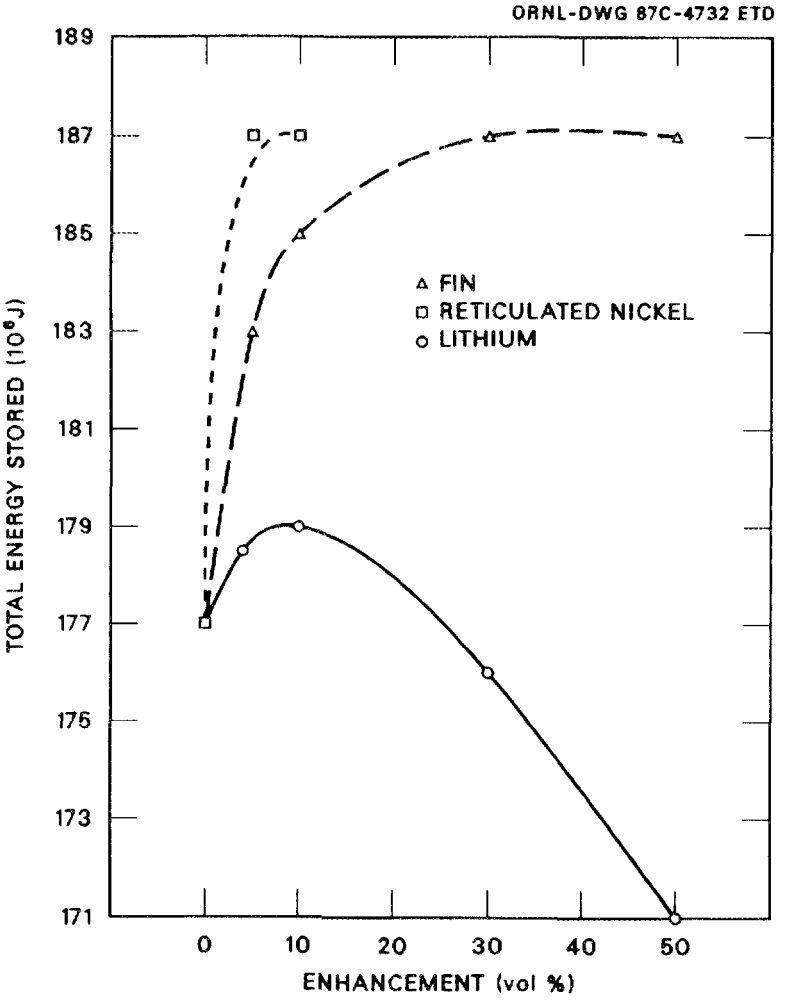

Fig. 4.3. Effect of Enhancements on Total Energy Storage.

storage a small amount for additions of 10% or less. Larger amounts of liquid lithium actually decreased the energy storage capacity. This decrease is attributable to the low density of liquid lithium, lower even than the PCM. Since the volume of each tube is held constant, increasing the proportion of liquid lithium decreases the mass of the PCM mixture. The opposite is true for the other enhancement options.

For the specified operating period range, the energy storage density is decreased by the use of fins and the reticulated nickel insert but was relatively unchanged by the addition of liquid lithium, see Fig. 4.4. The thin fin and nickel additions of 10% decrease the energy storage density by about 7%.

Figure 4.5 shows that a reticulated nickel insert with a 95% void fraction offers the best compromise between an increase in storage capacity and a relatively small decrease (~1%) in the energy storage

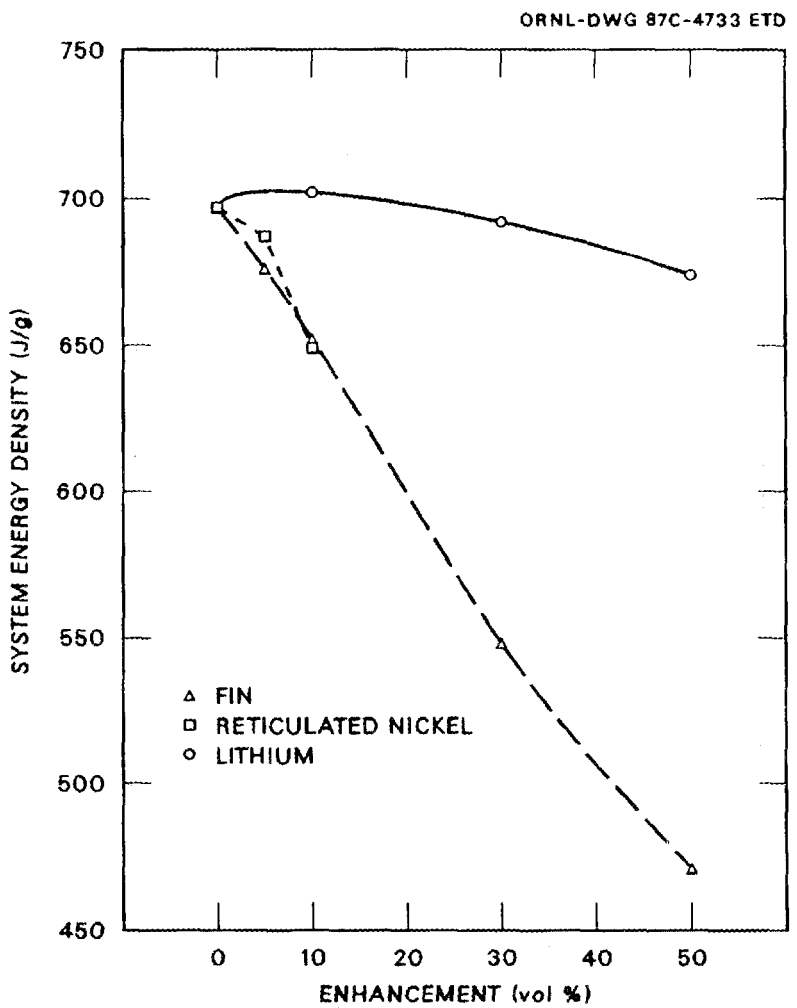

Fig. 4.4. Effect of Enhancements on System Energy Density.

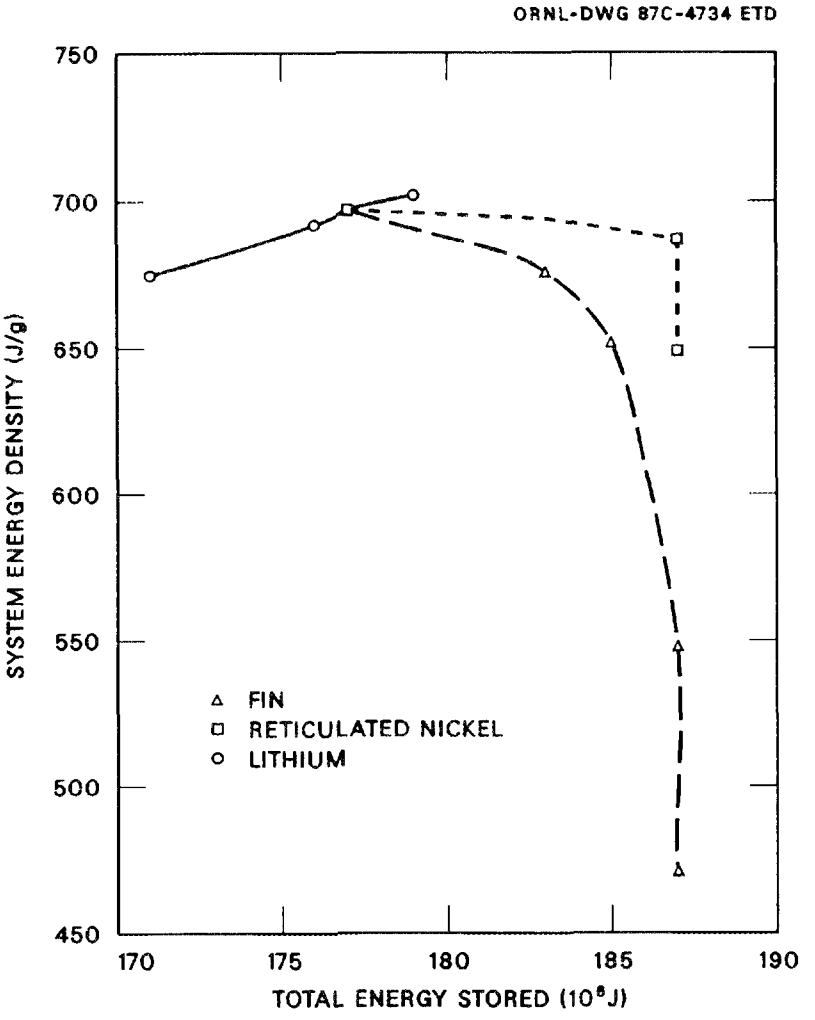

Fig. 4.5. System Energy Density vs Total Energy Stored for Enhanced Systems.

density for the specified operating period range. An addition of 10% liquid lithium increases both the energy storage density and the total energy storage capacity, but only by a very small amount. However, this option has the added benefit of reducing the hydrogen pressure of the lithium hydride PCM, as was discussed in Sect. 3.4.

The ratio of energy stored in the form of latent heat to the sensible heat within the PCM varies from 0.43 in the unenhanced configuration to 0.56 in the 90% void fraction reticulated nickel insert

configuration, as Table 4.2 shows. If all the unenhanced PCM, from an initial temperature of 700°K, were melted and at the melting temperature, this ratio would equal a value of 1.3. However, much of the PCM remains unmelted at the end of the operating period. Also, the PCM nearest the surface heats up above the melting temperature, further increasing the proportion of sensible heat storage.

The position of the phase change front at the end of the operating period is shown in Figs. 4.6 - 4.8. In these figures, the PCM

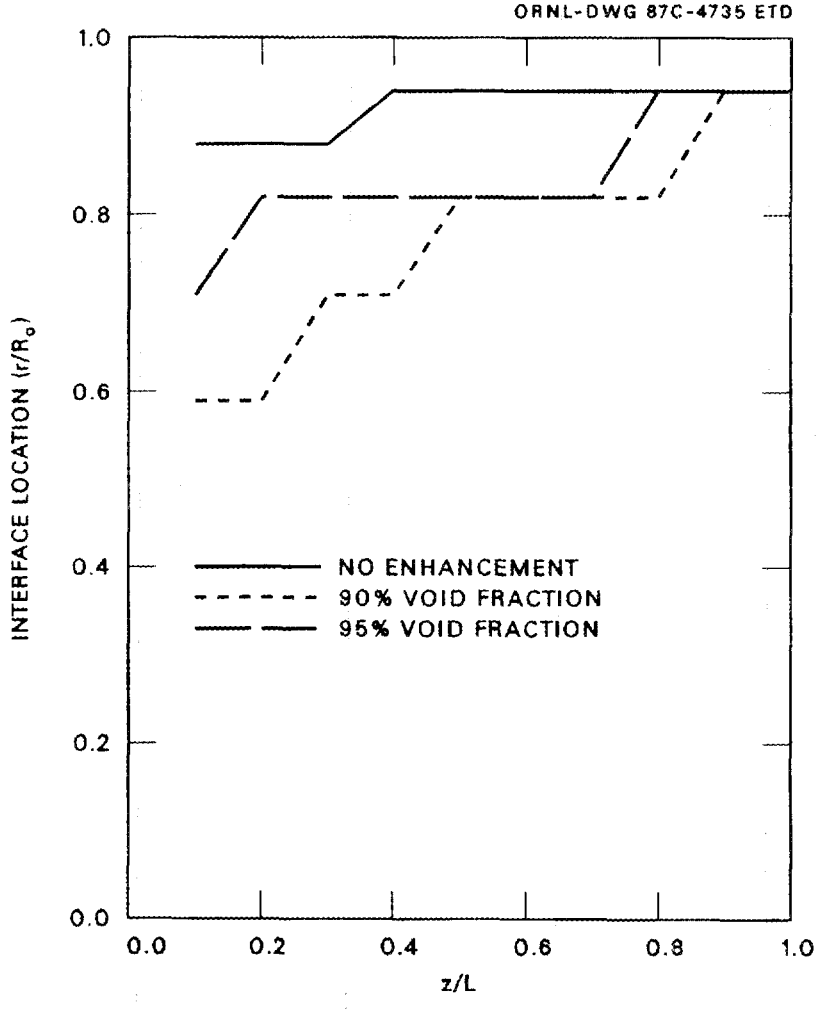

Fig. 4.6. Phase-Change Front Positions for Reticulated Nickel Enhancements.

Table 4.2. Performance Summary of Enhanced Systems[a]

Enhancement (volume %)	Thermal diffusivity (10^{-6} m^2/s)	FoSte[b]	Test[b] duration	System[c] energy density (J/g)	PCM[d] energy stored (10^6 J/tube)	θ*	Total energy[e] stored (10^6 J/tube)	Ratio of latent to sensible energy storage in the PCM	Ratio of energy stored in liquid metal to energy stored in PCM
				Reference case, no enhancement					
0	0.9	0.27	947	697	66.0	1.11	177	0.43	1.6
				Reticulated Nickel					
5	1.5	0.47	1000	687	76.7	1.35	187	0.53	1.4
10	2.0	0.69	1000	649	77.1	1.48	187	0.56	1.3
				Liquid lithium					
10	1.2	0.36	960	702	71.0	1.27	179	0.47	1.6
30	1.7	0.59	942	692	73.0	1.58	176	0.50	1.6
50	2.4	1.00	914	674	73.1	2.03	171	0.50	1.8
				304 SS thin fins					
5	1.1	0.36	978	676	72.4	1.26	183	0.47	1.5
10	1.4	0.46	992	652	75.8	1.38	185	0.50	1.4
30	2.3	0.97	1000	548	79.6	1.85	187	0.53	1.4
50	3.4	1.91	1000	471	81.7	2.52	187	0.48	1.4

[a] R_o = 0.05 m, R_f/R_o = 3, v = 0.04 m/s, L/D = 50, NPIPES = 4000.

[b] Computer model stops when liquid metal exit temperature reaches 1100°K or at 1000 s, whichever comes first.

[c] System includes liquid metal region and tube wall.

[d] Includes only enhanced PCM material.

[e] Includes energy stored in the form of increased internal energy of liquid metal in the annular region.

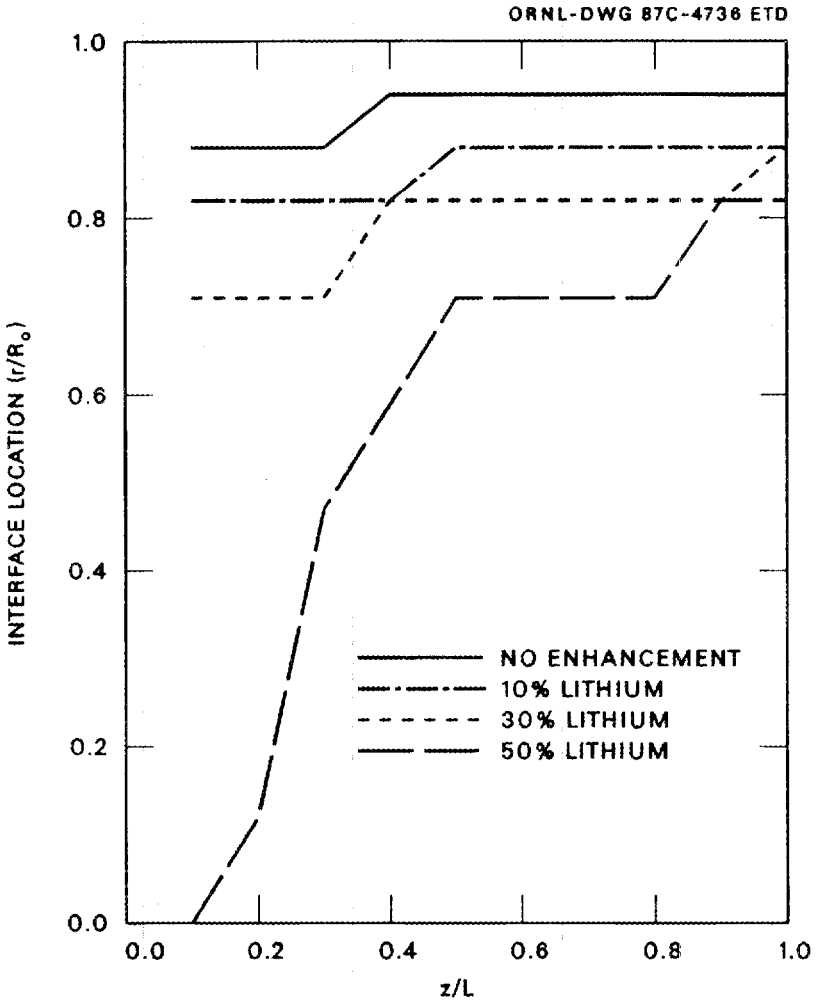

Fig. 4.7. Phase-Change Front Positions for Liquid Lithium Enhancements.

above the line is melted and the PCM below the line is solid. The stair-step appearance of these plots is caused by the nature of the finite difference solution and the size of the radial divisions. The front for most of the cases only penetrates about 25% of the way into the PCM. However, at an r/R_o value of .75, about 44% of the PCM volume is in the melted zone. The center of the PCM is melted only for very large additions of enhancement materials. Such large additions are not supported by the energy storage and energy density considerations already discussed.

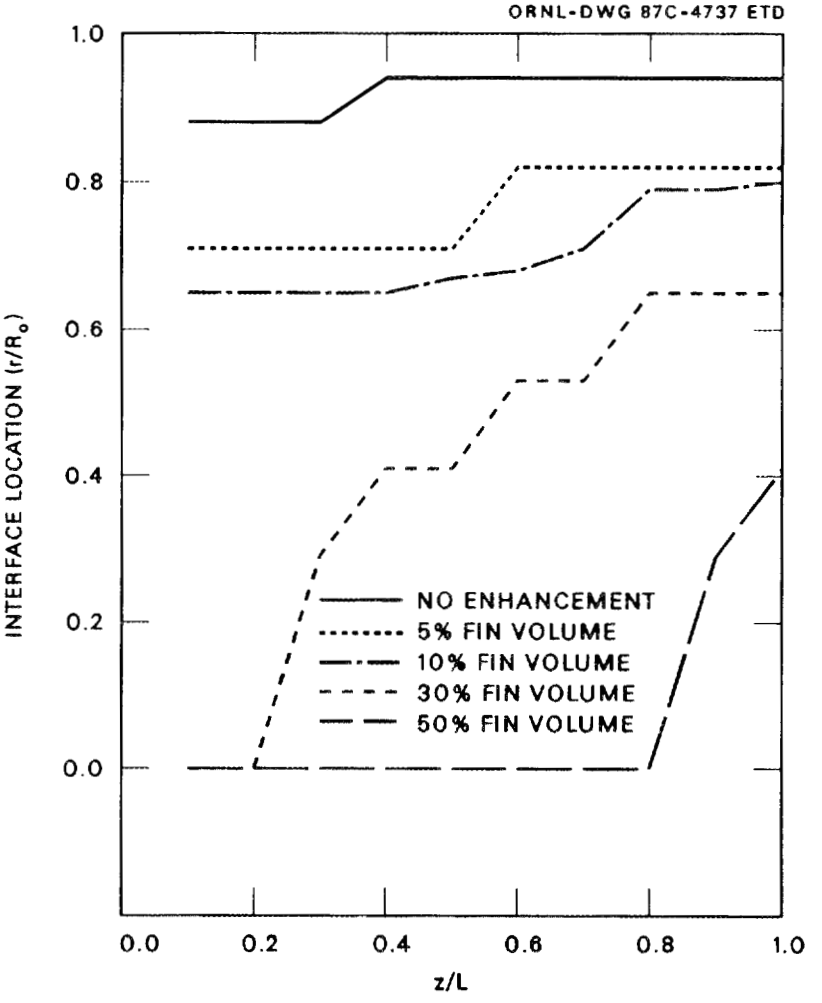

Fig. 4.8. Phase-Change Front Positions for 304SS Thin Fin Enhancements.

It is interesting to note, however, that doubling the volume percent of enhancement material from 5 to 10% has a relatively small effect on the interface location for both the reticulated nickel and thin fin cases, as does tripling the enhancement material from 10 to 30% in the liquid lithium case. However, tripling the fin volume from 10 to 30% has a very large effect, moving the interface all the way to the center of the PCM tube for $z/L < 0.2$. Increasing the fin volume by another 67% causes the melting front to reach the center for 80% of

the length of the tube. Also, increasing the liquid lithium fraction from 30 to 50% (only a 67% increase) causes a tremendous increase in melt front propagation for z/L <0.1.

Figure 4.9 shows the dimensionless temperature response of the central (r=0, z/L=.5) PCM node vs. the dimensionless time variable which reflects the varying Stefan numbers of the enhanced PCM. The nondimensional temperature response is slightly slowed by additional amounts of enhancement material (i.e., $\partial\phi/\partial$FoSte is decreased

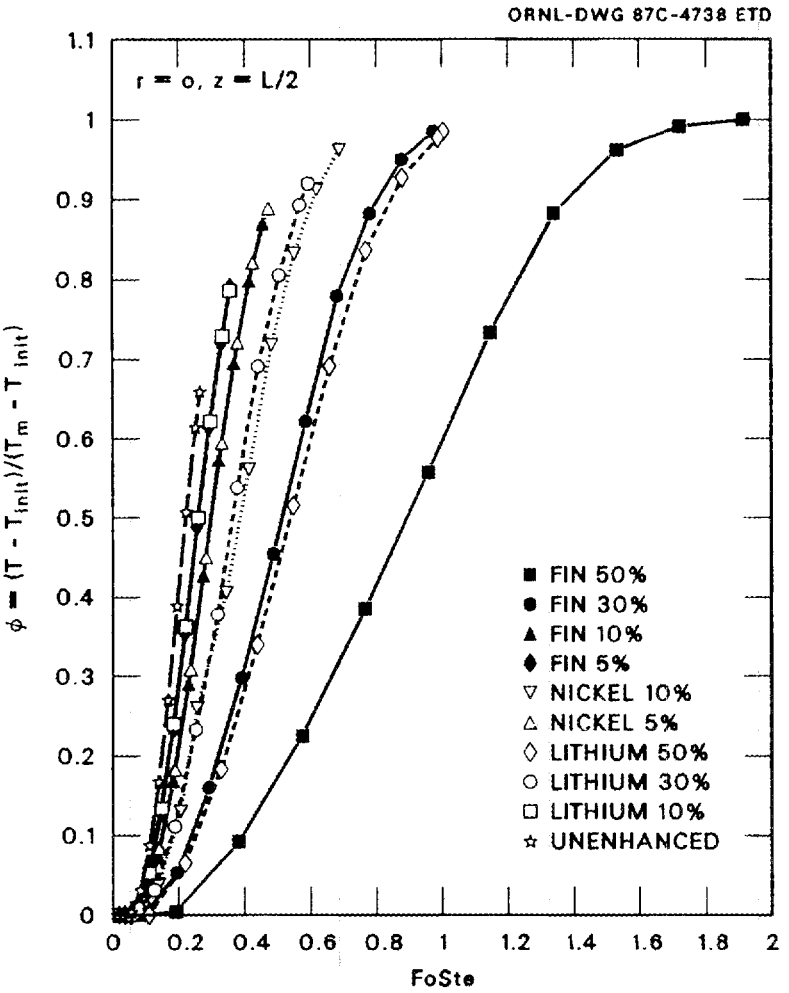

Fig. 4.9. Nondimensional Time Response of Central PCM Node for Enhanced Configurations.

as the thermal diffusivity is increased). The nondimensional behavior reflects the fact that the FoSte time parameter is proportional to the increasing thermal conductivity of the enhanced materials. This increasing thermal conductivity stretches the time scale, causing this counter-intuitive trend. However, for the real time data shown in Figs. 4.10-4.12, the time response is improved (i.e. $\partial T/\partial \tau$ is increased) by the addition of the enhancement materials.

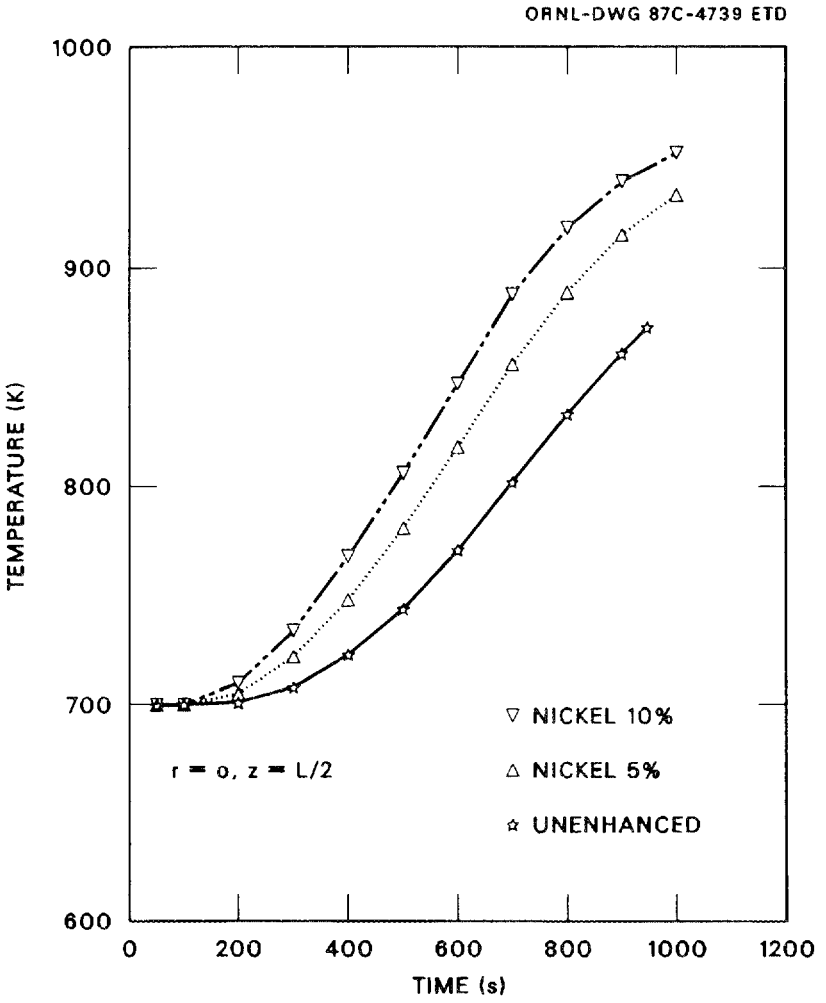

Fig. 4.10. Temperature Response of Central PCM Node for Systems Enhanced With Reticulated Nickel.

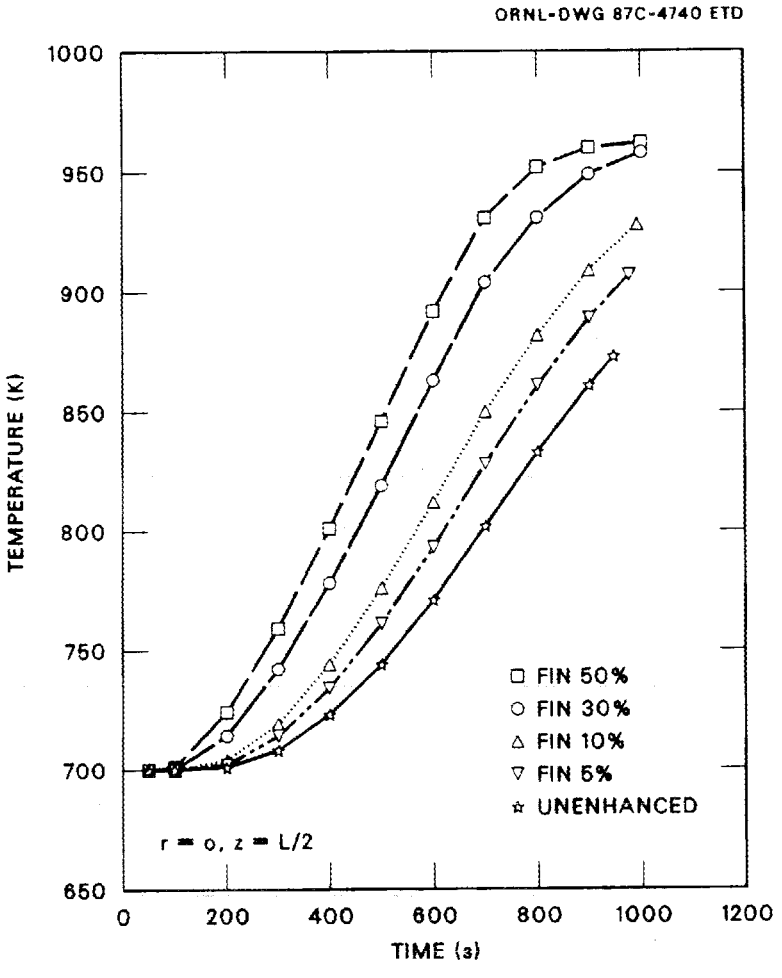

Fig. 4.11. Temperature Response of Central PCM Node for Systems Enhanced with 304SS Thin Fins.

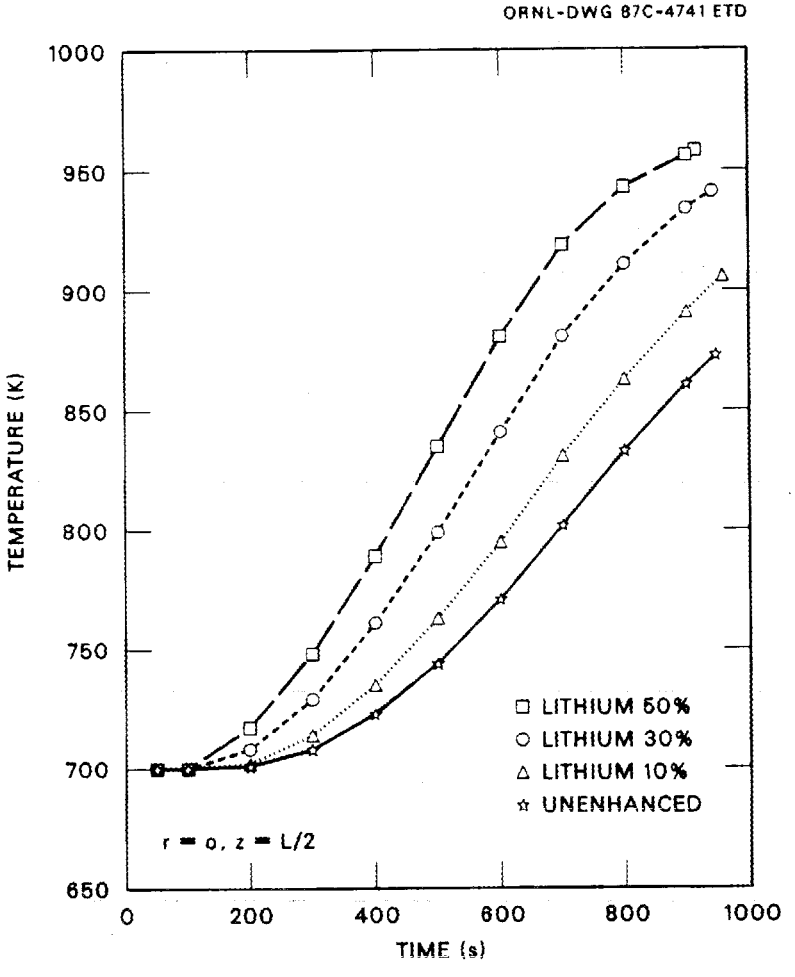

Fig. 4.12. Temperature Response of Central PCM Node for Systems Enhanced with Liquid Lithium.

4.3 Alternative Bases for Comparison

The performance comparisons reported in Sect. 4.2 were based on a strict adherance to the problem definition. Specifically, operating periods longer than 1000 seconds were not considered even though some of the enhanced systems were capable of receiving and storing further thermal energy without exceeding the liquid metal inlet and outlet temperature constraints. If the application of this thermal storage system was well defined and unlikely to change, this basis for comparison would be unquestioned. However, given the vagueness of the current applications requirements, further discussion of the performance of these systems is in order.

If the comparison were based solely on the system's physical dimensions and on the inlet and outlet liquid metal temperature constraints, several conclusions reached in Sect. 4.2 would be different as can be seen in Table 4.3.

For the reticulated nickel insert, the most important change is that now the total energy stored for the reticulated nickel insert continues to increase from 187 MJ to 197 MJ as the volume percent of nickel is increased from 5 to 10%. As the void fraction drops from 95 to 90%, the system energy density is decreased by only 20 J/g rather than the sharper drop of almost 40 J/g with the 1000 second limit. This would change the conclusion that the 95% void fraction material is clearly more effective than the 90% void fraction material. The choice between these two void fractions then becomes a more subtle trade-off between increased storage capacity, lengthened operating period, and slightly decreased system energy density.

Table 4.3. Alternative Performance Summary of Enhanced Systems[a]

Enhancement (volume %)	FoSte[b]	Test[b] duration	System[c] energy density (J/g)	PCM[d] energy stored (10^6 J/tube)	θ*	Total energy[e] stored (10^6 J/tube)	Ratio of latent to sensible energy storage in the PCM	Ratio of energy stored in liquid metal to energy stored in PCM
				Reticulated Nickel				
5	0.47	1000	687	76.7	1.35	187	0.53	1.4
5	0.48	1009	693	78.3	1.37	189	0.53	1.4
10	0.69	1000	649	77.1	1.48	187	0.56	1.3
10	0.72	1038	673	84.2	1.55	194	0.59	1.3
				304 SS Thin Fine				
30	0.97	1000	548	79.6	1.85	187	0.53	1.4
30	0.99	1013	556	82.2	1.89	190	0.54	1.3
50	1.91	1000	471	81.7	2.52	187	0.48	1.4
50	No change							

[a] R_o = 0.05 m, R_f/R_o = 3, v = 0.04 m/s, L/D = 50, NPIPES = 4000.

[b] Computer model stops when liquid metal exit temperature reaches 1100°K.

[c] System includes liquid metal region and tube wall.

[d] Includes only enhanced PCM material.

[e] Includes energy stored in the form of increased internal energy of liquid metal in the annular region.

The effect of this approach on the fin results is not as dramatic because the overall system energy density is still decreased substantially by the use of such fins. However, it becomes apparent that a maximum energy storage capacity occurs somewhere between 10 and 50% fin volume. The operating period is also slightly longer within this range.

Considering the changeable nature of these conclusions, some word of caution should accompany the results of this study. It would appear that the most appropriate system comparison should be based on optimized parameters for each enhanced system. However, such an optimization strategy is beyond the scope of this study. The development of such a strategy should be pursued if this type of thermal storage system remains a viable candidate in the overall system design.

5. CONCLUSIONS AND RECOMMENDATIONS

An approximate model of the PCM energy storage system was used to identify preliminary physical dimensions for the specified application. This specified application included a short charging period and the use of a liquid metal heat transfer fluid. A finite difference computer code was developed and used to evaluate the effect of three heat transfer enhancements on the PCM energy storage system.

For a maximum operating period of 1000 S, the use of a 95% void fraction reticulated nickel insert was found to increase the storage capacity of the system by ~6% with a decrease in the system energy density of only ~1%. For the given physical system, the storage capacity can be increased still further if the operating period is not constrained. The addition of 10% liquid lithium was found to cause minor increases in both storage density and storage capacity with the added benefit of reducing the hydrogen pressure of the lithium hydride PCM.

The unenhanced system that formed the basis of comparison for the various enhancements was not an optimized configuration. Based on a limited examination of other potential system configurations, significant performance improvements are possible. Such an optimization effort should be pursued if these configurations continue to be considered as candidate solutions. It also appears that a combination of a small addition of the liquid lithium might be considered in conjunction with the reticulated nickel, thereby gaining both the increased storage capacity and the reduced hydrogen pressure benefits of these two enhancements.

LIST OF REFERENCES

1. W. H. McCulloch, "Estimated Burst Power and Run Time Requirements for Representative SDI Weapons Platforms", Sandia National Laboratories, submitted to the Oak Ridge National Laboratory, July 8, 1987.

2. J. P. Foote, D. G. Morris, M. Olszewski, "Encapsulated Sink-Side Thermal Energy Storage for Pulsed Space Power Systems," 22nd Intersociety Energy Conversion Engineering Conference, Philadelphia, Pa., August 10–14, 1987.

3. Chapman, A. J., Heat Transfer, Fourth Edition, Macmillan Publishing Company, New York, 1987

4. M. Olszewski, D. G. Morris, Value of Energy Storage in Pulsed Space Power Systems, ORNL/TM-10530, Oak Ridge National Laboratory, in publication.

5. Foust, O. J. ed., Sodium-NaK Engineering Handbook, Vol II, Gordon and Breach, Science Publishers, Inc., New York, New York, 1976.

6. Solomon, A. D. et al., The Development of a Simulation Code for a Latent Heat Thermal Energy Storage System in a Space Station, ORNL-6213, Oak Ridge National Laboratory, Oak Ridge TN, April 1986.

7. N. Shamsundar and E.M. Sparrow, "Analysis of Multidimensional Conduction Phase Change Via the Enthalpy Model", Journal of Heat Transfer, Vol 97, pp. 333-340, August 1975.

8. G. M. Dusinberre, Heat Transfer Calculations by Finite Differences, International Textbook Co., Scranton, Pa., 1961.

9. T. R. Knowles and G.W. Webb, M/PCM Composite Thermal Storage Materials, American Institute of Aeronautics and Astronautics 22nd Thermophysics Conference, Honolulu, Hawaii, June 8-10, 1987, AIAA, New York, 1987.

10. O. E. Dwyer, On the Transfer of Heat to Fluids Flowing through Pipes, Annuli, and Parallel Plates, Nuclear Science and Engineering: p. 336-344 (1963).

11. L. Duchatelle, L. de Nucheze, M.G. Robin; J.C. Denton and N. H. Afgan, eds., Future Energy Production Systems, Vol 1, "Heat Transfer in Helical Tube Sodium Heated Steam Generators", Academic Press, 1976.

12. M. Valette, "A Heat Transfer Study for Vertical Straight-Tube Steam Generators Heated by Liquid Metal", Liquid Metal Engineering and Technology, Vol 2, Proceedings of the Third International Conference held in Oxford on 9-13 April 1984, British Nuclear Energy Society, London, 1984.

13. L. Duchatelle, L. de Nucheze, Determination des coefficients de convection d'un alliage sodium-potassium circulant a contre-courant dans un echangeur monotubulaire, Entropie no 17, 1967.

14. Kutateladze, S. S. et al, Liquid-Metal Heat Transfer Media, Consultants Bureau, Inc., New York, Chapman & Hall, Ltd., London, 1959.

15. V. I. Subbotin, et al., "Heat Removal from Reactor Fuel Elements Cooled by Liquid Metals," Proceedings of International Conference Peaceful Uses Atomic Energy, Third, Geneva, A conf. 28/p. 328, URSS, May 1964 (in Russian).

16. L. Duchatelle, et al, "Theoretical and Experimental Study of Phenix Steam Generator Prototype Modules", Nuclear Technology, Vol. 24, American Nuclear Society, Hinsdale, Illinois, November 1974.

17. Arpaci, V. S. and P. S. Larsen, Convection Heat Transfer, Prentice-Hall, Inc., Englewood Cliffs, New Jersey, 07632, 1984.

18. Forsythe, G. E. and W. R. Wasow, Finite-Difference Methods for Partial Differential Equations, John Wiley & Sons, Inc., New York, NY., 1960.

Internal Distribution

1. W. L. Asbury
2. L. Berry
3. D. W. Burton
4. J. A. Getsi
5. H. E. Guinn
6. C. E. Irwin
7. A. A. Kahn
8. S. C. Loggis
9. J. R. Merriman
10. D. G. Morris
11-15. M. Olszewski
16. L. T. Royer
17. C. M. Sigler
18. M. Siman-Tov
19. A. Soloman
20-24. T. K. Stovall
25. J. Tomlinson
26. H. E. Trammell
27. R. P. Wichner
28. G. E. Wrenn
29. ORNL Patent Office
30. Document Reference Section
31. Central Research Library
32-33. Laboratory Records Department
34. Laboratory Records (RC)

External Distribution

35. Office of Assistant Manager for Energy Research and Development, Department of Energy, ORO, Oak Ridge, TN 37831
36. E. B. Kennel, AFWAL/POOS, Wright-Patterson AFB, Ohio 45433
37-40. AFWAL/POOS, Aeronautical Laboratory, Wright-Patterson AFB, Ohio 45433
    W. Borger
    E. T. Mahefky
    J. Beam
    J. Johnson
41-42. EG&G Idaho, Inc./INEL, P.O. Box 1625, Idaho Falls, ID 83415
    R. Rice
    J. F. Whitbeck
    J. Martinell
43-44. GA Technologies, P.O. Box 85608, San Diego, CA 92138
    C. Fisher
    G. Fitzpatrick
45. R. Giellis, Martin Marietta Corp., P.O. Box 179, Denver, CO 80201
46-47. Sandia National Laboratory, Albuquerque, NM 87185
    W. H. McCulloch
    F. Wyant
48-49. NASA Lewis Research Center, 21000 Brookpark Road, Cleveland, OH 44135
    Ted Mroz
    J. Sovie, MS 301-5
50. R. Verga, SDI Organization, The Pentagon, Washington, DC 20301-7100
51. A. D. Schoenfeld, TRW, One Space Park, Redondo Beach, CA 90278

52. J. R. Wetch, Space Power Inc., 1977 Concourse Drive, San Jose, CA 95131
53. S. H. Winkler, Grumman Aircraft Systems, Bethpage, NY 11714-3582
54. E. Wahlquist, U.S. Department of Energy, NE-54, F415/GTN, Germantown, MD 20545
55. J. P. Foote, Dept. of Mechanical Engineering, U.T. Space Institute, Tullahoma, TN 37388
56. Dr. Leon Bledjian, Aerospace Corporation, Box 92957 D8/M4-916, Los Angeles, CA 90009
57. Dr. Scott Samuelson, San Francisco DOE Ops, 1333 Broadway, Oakland, CA 94612
58. Major Joe Sholtis, HQ DOE, NE-50, Washington, DC 20545
59. Dr. Roger K. Wedel, Lockheed Missile Sys. Corp., Dept. 51-21, B586, Box 3504, Sunnyvale, CA 94088-3504
60. Dr. Wen Chiu, General Electric VPSC, P.O. Box 8555, Philadelphia, PA 19101
61. Mr. Irvin Adler, Hughes Aircraft Company, P.O. Box 9919, Bldg. S-41, MS A315, Los Angeles, CA 90009
62. Dr. Howard Collicott, Boeing Aerospace Corp., P.O. Box 3999, MS 82-23, Seattle, WA 78124
63. Dr. Dave Buden, SDIO/SLKT, The Pentagon, Washington, DC 20301-7100
64. Capt. Mike Brasher, AFSTC/TPC, Kirtland AFB, NM 87117-6008
65. Mr. G. Allen Beale, RPL/LKCS, Edwards AFB, CA 93523
66. Mr. Leroy Herold, TRW Electronics & Defense, Bldg. 4, Rm. 2066, One Space Park, Redondo Beach, CA 90278
67. Mr. H. S. Bloomfield, NASA LeRC, MS 301-5, Cleveland, OH 44135
68. Dr. Richard E. Rice, USDOE Idaho Ops Office, P.O. Box 2245, Idaho Falls, ID 83403-2245
69. Robert Brengle, Rockwell International, 6633 Canoga Ave. Canoga Park, CA 91303
70. DTIC, Cameron Station, Alexandria, VA 22304-6145
71. AUL/LSE, Maxwell AFB, AL 36112
72. AFWAL/IMST, Bldg. 22, WPAFB, OH 45433
73. Dr. E. T. Curran, AFWAL/PS, WPAFB, OH 45433-6563
74. Michael R. Beltran, Beltran Inc., 1133 E. 35th St., Brooklyn, NY 11210
75. Dr. Michael Hsu, Ztek Corp., 400-2 Totten Pond Rd., Waltham, MA 02154
76. Javier A. Valenzuela, Creare, Inc., P.O. Box 71, Etna Road, Hanover, NH 03755
77. Ned S. Rasor, Rasor Associates, 253 Humboldt Ct., Sunnyvale, CA 94086
78. Dr. Jack Holman, Mechanical Engineering Dept., Southern Methodist University, Dallas, TX 55275
79. Dr. Nils Diaz, 202 NSC Univeristy of Florida, Gainesville, FL 32611
80. Dr. Dean Jacobson, Dept. of Chemical & Bio Engineering, Arizona State University, Tempe, AZ 85287
81. Mr. Bob Campana, ElectroTechnologies Corp., 11180 Roselle Ste G, San Diego, CA 92121

82. Roger Demler, Foster-Miller Corp, 350 Second Ave., Waltham, MA 02254
83. Harold T. Couch, HTC Inc., 11 Canaan Way, Simsbury, CT 06070
84. Jerome E. Toth, Thermacore Inc., 780 Eden Road, Lancaster, PA 17601
85. David Chittenden, L'Garde Inc., 1555 Placentia Ave., Newport Beach, CA 92663-2870
86. W. J. Carr, Jr., WJC ReSEARch and Development, 1450 Jefferson Hts., Pittsburgh, PA 15235
87. Dr. Mike Schuller, AFWL/AWYS, KAFB, NM
88-90. Mechanical Engineering Department, University of Tennessee, Knoxville, TN 37916
Prof. R. Arimilli
Prof. E. G. Keslock
Prof. M. Parang
91-100. Office of Scientific and Technical Information, P.O. Box E, Oak Ridge, TN 37831